ISSN 2427-4577

BULLETIN N° 231
ACADÉMIE EUROPEENNE INTERDISCIPLINAIRE DES SCIENCES
INTERDISCIPLINARY EUROPEAN ACADEMY OF SCIENCES

Lundi 7 janvier 2019 :
à 16h
à l'Institut Henri Poincaré salle 01
11, rue Pierre et Marie Curie 75005 PARIS/Métro : RER Luxembourg

Conférence : "*Topologie et physique quantique mésoscopique*"
Par Christophe MORA, Maître de Conférences Université Paris VII Diderot
Laboratoire Pierre Aigrain département de Physique ENS

Notre Prochaine séance aura lieu le lundi 4 février 2019 à 15h30
à l'Institut Henri Poincaré salle 421
11, rue Pierre et Marie Curie 75005 PARIS/Métro : RER Luxembourg

Elle aura pour thème

1. **Examen de candidatures**
2. **Conférence :**

"*Simulations de dynamique moléculaire:*
***un microscope numérique pour sonder la matière à l'échelle atomique.*"**
Par Rodolphe VUILLEUMIER , Pr classe exceptionnelle SORBONNE UNIVERSITÉ (SU)
Directeur Laboratoire PASTEUR Unité mixte de Recherche CNRS-ENS-SU

ACADÉMIE EUROPÉENNE INTERDISCIPLINAIRE DES SCIENCES
INTERDISCIPLINARY EUROPEAN ACADEMY OF SCIENCES

Janvier 2019

N°231

TABLE DES MATIERES

Prochaine séance : lundi 4 février 2019

Conférence :

"*Simulations de dynamique moléculaire: un microscope numérique pour sonder la matière à l'échelle atomique.*"

Par Rodolphe VUILLEUMIER , Pr classe exceptionnelle SORBONNE UNIVERSITÉ (SU)
Directeur Laboratoire PASTEUR Unité mixte de Recherche CNRS-ENS-SU

ACADEMIE EUROPEENNE INTERDISCIPLINAIRE DES SCIENCES

Fondation de la Maison des Sciences de l'Homme, Paris.

Séance du Lundi 7 janvier 2019/IHP 16h

La séance est ouverte à 16h **sous la Présidence de Victor MASTRANGELO** et en la présence de nos Collègues Gilbert BELAUBRE, Jean BERBINAU, Jean-Louis BOBIN, Eric CHENIN, Gilles COHEN-TANNOUDJI, Françoise DUTHEIL, Claude ELBAZ, Jean -Pierre FRANCOISE, Michel GONDRAN, Irène HERPE-LITWIN, Claude MAURY, Marie-Françoise PASSINI, Jacques PRINTZ, Jean SCHMETS, Michel SPIRO, Jean-Paul TEYSSANDIER, Jean-Pierre TREUIL .

Etaient excusés :François BEGON, Jean-Pierre BESSIS, Bruno BLONDEL, Jean-Louis BOBIN, Michel CABANAC, Alain CARDON, Juan-Carlos CHACHQUES, Alain CORDIER , Daniel COURGEAU, Ernesto DI MAURO, Jean-Felix DURASTANTI, Vincent FLEURY, Robert FRANCK, Jacques HENRI-ROBERT, Dominique LAMBERT, Gérard LEVY, Pierre MARCHAIS, Anastassios METAXAS, Jacques NIO, Edith PERRIER, Pierre PESQUIES, Alain STAHL, Jean VERDETTI.

Etait présent notre collègue membre correspondant Benoît PRIEUR

Etaient présents en tant que visiteurs Denise et René PUMAIN,

I. Présentation du conférencier par notre Président Victor MASTRANGELO.

Christophe MORA est depuis 2006 Maître de conférence à l'Université Paris Diderot 7. Il est affecté au Laboratoire Pierre Aigrain du département de Physique de l'ENS.

Formation:

Ancien élève de l'ENS Paris, (1997-2000) , il a soutenu en 2003 une Thèse de l'université Paris VI, Laboratoire de Physique statistique (ENS Paris), intitulée "*Gaz de fermions et de bosons condensés : phases de Fulde-Ferrell-Larkin-Ovchinnikov et quasicondensats"*, avec pour Directeurs Roland COMBESCOT et Yvan CASTIN et obtenu en 2012 son habilitation à diriger des recherches à l'Université Paris VII Diderot.

Il a été membre des comités **HCERES** de l'INAC (Institut Nanosciences et Cryogénie), Grenoble, janvier 2015 ; et du LOMA (Laboratoire Ondes etMatière d'Aquitaine), Bordeaux, février 2015.

Responsabilités collectives

Il a été membre du jury de 7 thèses. Il a également été membre des groupes d'experts thématiques (GET) *Dispositifs quantiques* (2009-2012), puis *nanoquantique* (2012-) de l'UFR de physique de Paris Diderot 7 et Co-responsable du GET *nano-quantique* (2012-) et Membre du conseil des enseignements , UFR de physique Paris Diderot (2016-) **.**

Il a été **Referee** régulier pour les journaux *Nature Physics*, *Physical Review Letters*, *Physical Review A*, *Physical Review B* et *The European Physical Journal B.*

Activités d'Enseignement :

Responsabilités d'UE

2013- Mathématique S5 (en L3 magistère puis L3 général)
2009-2012 Mathématique en L1 SNV (Département des Sciences de la Nature et de la Vie).

Matières enseignées: Physique numérique (M1), Fermions et bosons fortement corrélés (M2), Physique statistique (L3 et M1), Mathématiques pour physiciens (L3), Théorie de la matière condensée (M2), Electromagnétisme(TP L2), Mécanique (L1), électronique Numérique (TP L3), Mathématiques pour biologistes(L1), Physique statistique et transition de phases (M2), Statistiques quantiques (M2), Électronique analogique (TP et TD L3), Optique (TP, L3 Pro), Électrostatique (L2)

Il a également accompagné dans leurs recherches de nombreux post-doctorants ...

Ses principales thématiques de recherche sont:

- Électrodynamique quantique et optique quantique des circuits, interaction transport électronique rayonnement.
- Fermions de Majorana , parafermions, topologie, supraconductivité, systèmes unidimensionels (Luttinger), désordre.
- Physique mésoscopique et corrélations fortes, impuretés quantiques, effet Kondo et modèle d'Anderson,dynamique électronique et transport hors-équilibre dans les conducteurs quantiques.
- Atomes ultra-froids , gaz fermioniques déséquilibrés, gaz de Bose en interaction, effet Efimov et physique à trois ou quatre corps, confinement et basses dimensions, transition solide-superfluide.

Publications:
Il est l'auteur de **54 publications** dans des revues à comité de lecture (quatre soumises sur arXiv) dont **1** dans **S**cience, 2 dans Nature Physics, 13 dans Phys. Rev. Lett., 2 dans New J. Phys., 2 dans Europhys. Lett., 1 dans Rep. Progr. Phys., 25 dans Phys. Rev. B, 3 dans Phys. Rev. A, 3 dans C. R. Physique, 2 dans Eur. Phys. J. B.

Conférences:
Il été invité à 15 conférences et a fourni 7 contributions orales.

II. Conférence de Christophe MORA "*Topologie et physique quantique mésoscopique*"

Résumé de la conférence:

Résumé :

La topologie est une branche des mathématiques étudiant les déformations continues d'objets et leurs invariants. Son utilisation en physique a toujours été très fructueuse en permettant notamment d'identifier des structures robustes et universelles. Elle s'est fortement accélérée depuis un peu plus d'une dizaine d'année lorsque les physiciens ont réalisé que la topologie jouait un rôle très important dans la caractérisation des fonctions d'onde électroniques dans les matériaux solides. Un prix Nobel, celui de 2016, est venu couronner cette recherche en physique s'appuyant sur des concepts de topologie.

Nous discuterons quelques notions de topologie et leurs liens avec l'application de la physique quantique aux électrons dans les solides. Nous verrons de quelle manière la topologie explique l'apparition de phénomènes robustes dans le cadre de la physique mésoscopique.

Un compte-rendu détaillé, voire **un enregistrement audio-vidéo** sera prochainement disponible sur le site de l'AEIS http://www.science-inter.com.

REMERCIEMENTS

Nous tenons à remercier vivement Mme Sylvie BENZONI Directrice de l'Institut Henri POINCARE et Mmes Florence LAJOINIE et Chantal AMOROSO ainsi que les personnels de l'IHP pour la qualité de leur accueil.

Documents

- Pour préparer la conférence du Pr Rodolphe VUILLEUMIER , nous vous proposons :

p 07 : un résumé de sa conférence " *Simulations de dynamique moléculaire: un microscope numérique pour sonder la matière à l'échelle atomique***.**"

p 08 : un article de Rodolphe VUILLEUMIER et al. intitulé " Carbon dioxide transport in molten calcium carbonate occurs through an oxo-Grotthuss mechanism via a pyrocarbonate anion" paru dans NATURE CHEMISTRY | VOL 8 | MAY 2016 454 | www.nature.com/naturechemistry

- Pour compléter la conférence de Christophe MORA nous vous proposons:

p.15 : un article de Christophe MORA et al. intitulé "*Braiding Majorana zero modes using quantum dots*" de Corneliu Malciu, Leonardo Mazza, Christophe Mora, paru dans Phys. Rev. B 98, 165426 (2018)

Résumé de la conférence du Pr Rodolphe VUILLEUMIER

Simulations de dynamique moléculaire: un microscope numérique pour sonder la matière à l'échelle atomique.

Résumé:

Dans de nombreux domaines, les simulations numériques ont ouvert une troisième voie entre la méthode théorique et la méthode expérimentale. Ceci est particulièrement le cas dans le domaine de la chimie et de la science des matériaux. Les simulations de dynamique moléculaire ont apporté une vision nouvelle de la structure et de la dynamique à l'échelle atomique de systèmes aussi variés que les liquides, l'eau en particulier, les systèmes biologiques, les matériaux etc., allant parfois jusqu'à revoir la notion d'espèces chimiques. Dans cet exposé, nous commencerons par introduire ce que sont les simulations de dynamique moléculaire puis discuterons quelques unes de leurs applications que nous avons menées avec un accent particulier sur les solutions aqueuses et les systèmes géologiques. Enfin, nous présenterons quelques uns des développements en cours pour dépasser les frontières actuelles.

ARTICLES
PUBLISHED ONLINE: 29 FEBRUARY 2016 | DOI: 10.1038/NCHEM.2450
nature chemistry

Carbon dioxide transport in molten calcium carbonate occurs through an oxo-Grotthuss mechanism via a pyrocarbonate anion

Dario Corradini[1,2,3], François-Xavier Coudert[4]* and Rodolphe Vuilleumier[1,2,3]*

The reactivity, speciation and solvation structure of CO_2 in carbonate melts are relevant for both the fate of carbon in deep geological formations and for its electroreduction to CO (to be used as fuel) when solvated in a molten carbonate electrolyte. In particular, the high solubility of CO_2 in carbonate melts has been tentatively attributed to the formation of the pyrocarbonate anion, $C_2O_5^{2-}$. Here we study, by first-principles molecular dynamics simulations, the behaviour of CO_2 in molten calcium carbonate. We find that pyrocarbonate forms spontaneously and the identity of the CO_2 molecule is quickly lost through O^{2-} exchange. The transport of CO_2 in this molten carbonate thus occurs in a fashion similar to the Grotthuss mechanism in water, and is three times faster than molecular diffusion. This shows that Grotthuss-like transport is more general than previously thought.

Carbonatite melts, mostly composed of XCO_3 (X = Li_2, Na_2, K_2, Mg, Ca), have recently received a great deal of attention[1,2]. It has been proposed that they are the most conductive phase in Earth's upper mantle, and they may determine the mobility and long-term storage of deep carbon, especially if found in the lower mantle[3–5]. Analysis of conductivity data has led to estimations of a 0.035–0.35% content of carbonatites by volume in the asthenosphere, in line with the estimated CO_2 content in magmas[1]. CO_2 from geological formations is mostly released into the atmosphere during volcanic activity, although the efficiency of CO_2 degassing remains poorly known[6]. Despite the importance of CO_2 species for the deep carbon cycle[7], the reactivity, speciation and solvation structure of CO_2 in carbonatite melts have so far remained unexplored.

New technologies capable of reducing the carbon footprint are greatly in demand, in particular to limit the impact of CO_2 on the environment. One of the strategies considered in the context of carbon capture and valorization consists of its dissolution in a molten carbonate medium and its subsequent electroreduction to CO[8–10]. The interaction between CO_2 and carbonates is thus relevant for environmental science and engineering beyond geochemistry.

In the context of the electrochemical reduction of CO_2, it has been observed that the solubility of CO_2 in the carbonate electrolyte is higher than would be expected simply from the expression $x^l_{CO_2} = k_H P_{CO_2}$, where $x^l_{CO_2}$ is the concentration of CO_2 in the liquid, k_H is Henry's constant and P_{CO_2} is the CO_2 partial pressure. To explain this increased solubility, a reaction of CO_2 with the carbonate anion has been hypothesized:

$$CO_2 + CO_3^{2-} \rightleftharpoons C_2O_5^{2-} \quad (1)$$

with the product of the reaction being called pyrocarbonate (or dicarbonate)[8–10]. Taking K_{pyro} as the equilibrium constant of this chemical reaction, one can then define an apparent Henry's constant $k_H^{app} = (1 + K_{pyro})k_H$. Thus it is possible that the CO_2/pyrocarbonate equilibrium controls the solubility of CO_2 in molten carbonates. Although this equilibrium can contribute to a larger CO_2 uptake in molten carbonates, it is not clear whether this is favourable for electrochemical processes, as the CO_2 involved in pyrocarbonate may not be readily accessible depending on the rate of interconversion. It is thus crucial to obtain a better understanding of CO_2 solvation in molten carbonates at the molecular level.

A limited number of previous studies have provided some support to the possibility of the formation of pyrocarbonate. The existence of a CO_2/pyrocarbonate equilibrium was first hypothesized by Claes and colleagues on the basis of experiments performed on the Li–Na–K carbonate eutectic mixture[11]. This has also been supported by gas-phase calculations[12]. It was later shown, using density functional theory (DFT) calculations, that in the gas phase $C_2O_5^{2-}$ and larger oligomers $C_nO_{2n+1}^{2-}$ are structurally stable, with their energetics being strongly dependent on the counterion[13]. Polymeric phases of CO_2 have also been predicted by DFT[14]. Zhang and co-workers have provided evidence of the presence of pyrocarbonate in Raman spectroscopy experiments, performed by exposing molten carbonate mixtures to a CO_2 atmosphere[15]. Finally, pyrocarbonate has also been invoked to explain NMR spectra in aqueous carbonate solutions[16].

Recently, two first-principles molecular dynamics (FPMD) studies have addressed the properties of molten carbonates[17] and of CO_2 in silicate melts[18]. The first study provided information relevant for the study of liquid $CaCO_3$, until then poorly explored in experiments, such as its liquid structure, density, atomic vibration motions, diffusion coefficients and electrical conductivity. In the second, the speciation of CO_2 in basaltic and kimberlitic melts in the CaO–MgO–Al_2O_3–SiO_2 system was investigated. Importantly, the formation of $C_2O_5^{2-}$ has been observed in the basaltic melt, accounting for ~3.7% of the C content in the system. Pyrocarbonate has been found to be a transient species with a very short mean lifetime of 175 fs, too short to assess its solvation structure and formation/dissociation dynamics.

In this study, we focus on CO_2 in molten $CaCO_3$, with the aim of characterizing the formation/dissociation of the pyrocarbonate and the solvation structure of CO_2 and pyrocarbonate in the melt. Using

[1]Department of Chemistry, École Normale Supérieure - PSL Research University, 24 rue Lhomond, 75005 Paris, France. [2]Sorbonne Universités, UPMC Univ. Paris 06, PASTEUR, 75005 Paris, France. [3]CNRS, UMR 8640 PASTEUR, 75005 Paris, France. [4]PSL Research University, Chimie ParisTech – CNRS, Institut de Recherche de Chimie Paris, 75005 Paris, France. *e-mail: fx.coudert@chimie-paristech.fr; rodolphe.vuilleumier@ens.fr

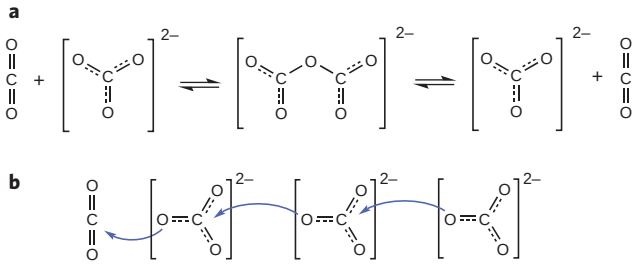

Figure 1 | Oxo-Grotthus mechanism via a pyrocarbonate anion. **a**, Formation of the pyrocarbonate ion $C_2O_5^{2-}$ from the reaction of CO_2 with carbonate anion CO_3^{2-}. **b**, A cascading mechanism, with rapid sequence of pyrocarbonate formation and dissociation events.

FPMD simulations, we confirm the presence of pyrocarbonate, which exists in rapid exchange with separate CO_2 and carbonate. The pyrocarbonate ion lives longer in $CaCO_3$ than in the basaltic melt reported in ref. 18, allowing us to study the details of its solvation structure, beyond its geometry. In addition, we find that the transport of CO_2 in molten carbonate occurs in a manner similar to the Grotthuss mechanism for proton transport in water, via independent events of formation and dissociation of the pyrocarbonate molecule.

Results and discussion

Formation of pyrocarbonate anion. Using FPMD simulations, we studied the behaviour of one CO_2 molecule in the $CaCO_3$ solvent. From analysis of the simulation trajectory, we observed the spontaneous formation of the pyrocarbonate ion $C_2O_5^{2-}$ out of the reaction of CO_2 with the carbonate anion CO_3^{2-}, as shown in Fig. 1a. There is a rapid exchange between the species, with multiple instances of formation and dissociation of the pyrocarbonate ion (79 events each in the simulation time span of 65 ps). To define the molecular species from the FPMD simulation trajectory, it is necessary to use a distance criterion, usually determined by looking at the minimum of the pair radial distribution functions (RDFs). We used a 'hysteresis' criterion with minimal/maximal C–O* distances, where O* is the central pyrocarbonate ion linking the two C atoms, C–O*–C (the other oxygen atoms in pyrocarbonate are simply termed O in the following; see Methods for further details). The minimal/maximal distances considered were 1.7 Å/1.95 Å, because within this span the C–O pair RDF is practically zero for molten carbonates.

With the abovementioned criteria we observed the presence of pyrocarbonate in the simulation box during 24.4% of the total simulation time. From this we can estimate a free energy of formation of $\Delta A = RT\ln((1-p_{pyro})/p_{pyro}) = 16.8 \pm 1.4$ kJ mol^{-1} ($RT = 14.7$ kJ mol^{-1} at $T = 1{,}773$ K). The minimal/maximal intervals for the continual presence of CO_2 or pyrocarbonate are 0.024 ps/4.84 ps and 0.016 ps/1.52 ps, respectively. By analysing the histograms of the durations of CO_2 or pyrocarbonate intervals (Supplementary Fig. 1), we estimate a CO_2 average lifetime of $\tau_{CO_2} = 0.88$ ps and a pyrocarbonate average life time of $\tau_{pyro} = 0.28$ ps.

The snapshots presented in Fig. 2a–c show, respectively, the approach of CO_3^{2-} to CO_2, the formed pyrocarbonate, and its dissociation to CO_3^{2-} and CO_2. As we can see in Fig. 2d, the identity of the C atoms belonging to the CO_2 or pyrocarbonate varies along the simulation trajectory. We thus looked at all the pyrocarbonate formation/dissociation events and kept track of the C atom part of the CO_2 molecule before the formation of pyrocarbonate and after its dissociation. We found that 72.2% of the time the same C is part of CO_2 before and after a pyrocarbonate ion time interval. Conversely, this means that 27.8% of the time a different C atom is part of the CO_2 after dissociation of the pyrocarbonate.

To go further, we measured the correlation between events in which the C remained the same and between events in which the C changed. Given an event where the C remained the same before the formation and after the dissociation of pyrocarbonate, we measured the frequency of occurrence of n (after the first) consecutive events of the same kind. We also did the same for events where the C had instead changed before the formation and after the dissociation of pyrocarbonate. The results are shown in Fig. 2e, which also plots the theoretical curves $\gamma(1-\gamma)^n$ for 'stay' events and $(1-\gamma)\gamma^n$ for 'change' events, with $\gamma = p_{stay\to change} = p_{stay}(0)$, which assumes no correlation between successive events. The probability of n consecutive 'stay' events is a slowly decaying function of n. Conversely, the probability of consecutive 'change' events decays very rapidly, with a small probability of another change in C after the first one and a very small probability of having two changes after the first one. The cascading of C transfers, through a rapid succession of jump events (as in Fig. 1b), therefore appears unlikely. Hence, in the carbonate melt, the transport of CO_2 (free or bound in pyrocarbonate form) occurs via independent events of formation/dissociation of the pyrocarbonate molecule. This is similar to the Grotthuss mechanism in water, which involves the Zundel cation, $H_3O^+ + H_2O \rightleftharpoons H_5O_2^+$, with oxygen playing the role of the proton. By a random walk model, we estimate the diffusion coefficient of CO_2 to be $D_{Grotthuss} = 8.3 \times 10^{-9}$ m^2 s^{-1}, that is, 2.8 times faster than molecular diffusion of CO_2 (see Supplementary Information for details). It would be of interest in future work to verify, in the presence of an external electric field, whether a cascade of C transfer is likely to occur, similar to the correlated H transfers that have been observed in water under intense electric fields[19].

Pyrocarbonate geometry. Having observed that the pyrocarbonate ion exists in a significant portion of our simulation run, we then proceeded to characterize its geometry by measuring distances and angles, as shown in Fig. 3. Figure 3a plots the distribution of C–C, C–O and C–O* distances. The C–O distribution is quite narrow, peaking at ~1.26 Å, while the C–C and C–O* distance distributions are quite wide. The latter has an asymmetric shape, which is related to the criterion chosen to define the pyrocarbonate molecule (see Methods for more details). Figure 3b shows the normalized distributions of the C–O*–C, O–C–O and O–C–O* angles for pyrocarbonate. The O–C–O and O–C–O* distributions are narrower, while the C–O*–C has a larger dispersion. This suggests that the central C–O*–C bridge is remarkably flexible. For comparison, we also show the O–C–O angle distribution for CO_3^{2-} molecules, which is narrow and peaks at ~120°. In the inset of Fig. 3b, we also show the logarithm of the normalized distribution of the O–C–O angle of the CO_2 molecule and compare it with the case of CO_2 in the gas phase (see Methods). Note that the fluctuations of the O–C–O angle are significantly enhanced in the condensed phase with respect to the gas phase. In fact, the O–C–O angle can even bend to ~120°. Despite the low polarizability of CO_2, we see here that the interactions with the surrounding medium, in this case composed of doubly charged cations and anions, can influence deeply the geometry of CO_2. In particular, the bending of the O–C–O can be related to its interaction with CO_3^{2-} and formation of the pyrocarbonate. Indeed in pyrocarbonate, we observe a O–C–O angle distribution peaking at ~130°.

Supplementary Table 1 compares the mean values of the distances and angles in the pyrocarbonate molecule found in our study with those obtained in silicate melts[18] and in the gas phase, as studied using MP2 calculations by Peeters and co-authors[12]. The extracted values in the $CaCO_3$ solvent are quite similar to those that have been found in silicate melts. The geometry of the pyrocarbonate ions thus appears to stay approximately constant in

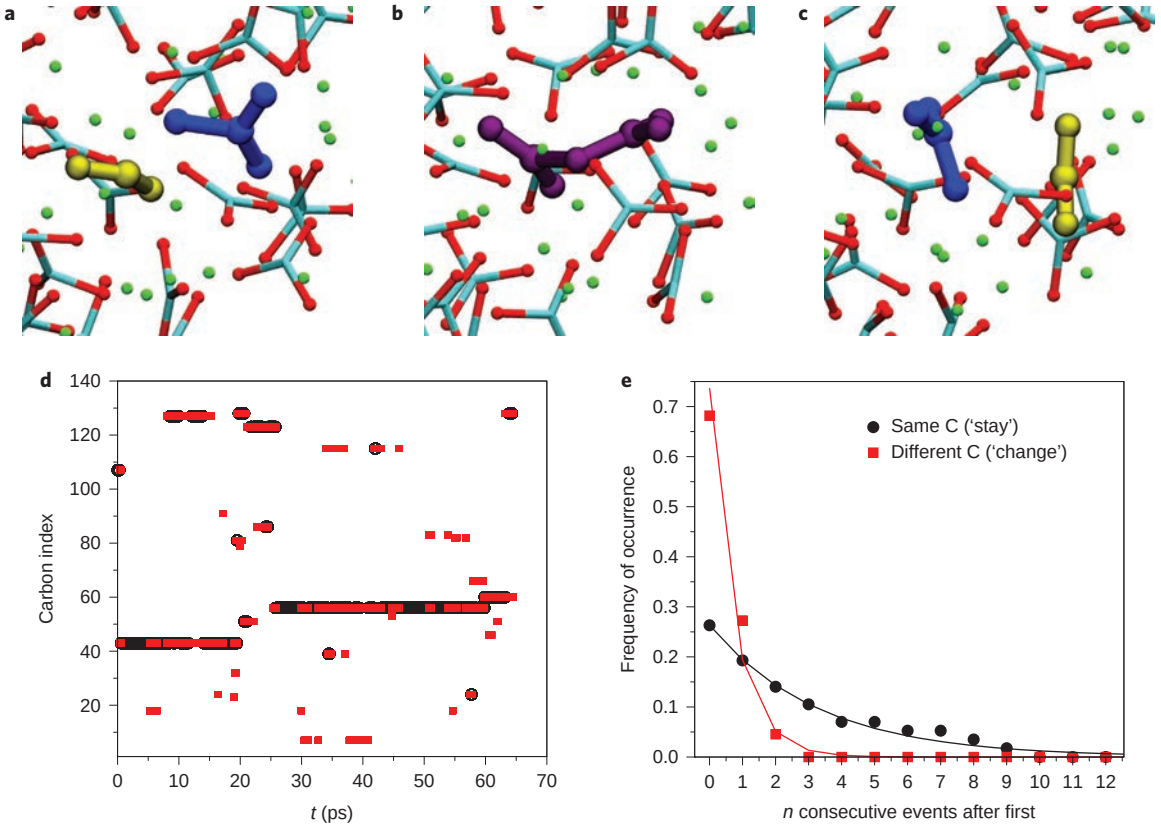

Figure 2 | Formation/dissociation of pyrocarbonate and C transport. a–c, Snapshots representing one instance of the formation/dissociation of pyrocarbonate during the simulation run: CO_2 and CO_3^{2-} approach (**a**), pyrocarbonate $C_2O_5^{2-}$ is formed (**b**) and pyrocarbonate dissociates into CO_3^{2-} and CO_2 (**c**). Carbonate molecules in the solvent are represented by cyan/red sticks, O atoms by red spheres and Ca atoms by green spheres. The CO_2 molecule is shown in yellow, the CO_3^{2-} molecule in blue, and pyrocarbonate in purple. **d**, Indices of the C atoms in CO_2 (black) and pyrocarbonate (red) along the simulation. **e**, The C atom in CO_2 is followed before the formation and after the dissociation of pyrocarbonate. The probability of that C atom staying the same, *n* consecutive times (always reforming the same CO_2 molecule), is shown in black, and the probability of it changing *n* consecutive times (cascading C transfers) is shown in red. The lines are as described in the text.

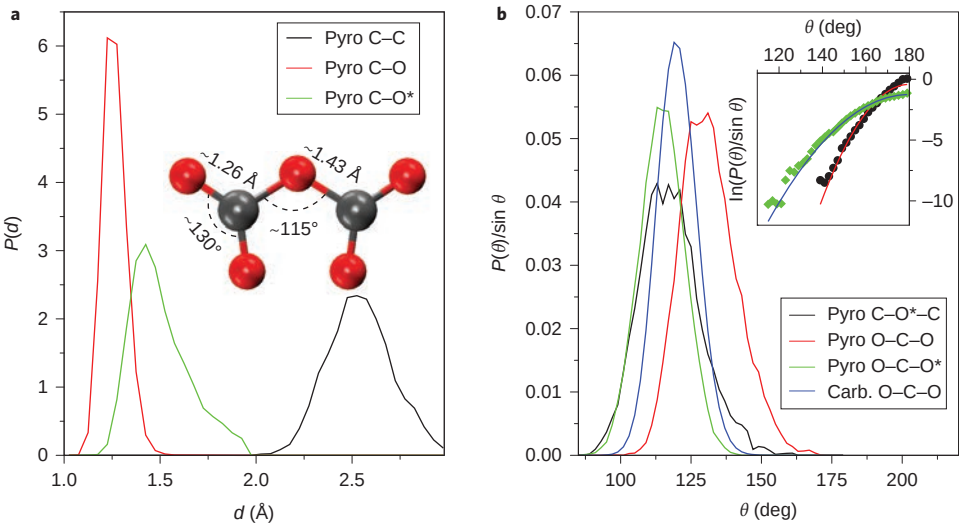

Figure 3 | Geometry of pyrocarbonate anion. a, Distribution of C–C, C–O and C–O* distances measured during the time intervals of existence of $C_2O_5^{2-}$. Inset: average geometry of pyrocarbonate (O, red; C, grey), with values of C–O* and C–O distances and C–O*–C and O–C–O angles shown. **b**, Distribution of C–O*–C, O–C–O and O–C–O* for the pyrocarbonate ion. For comparison, the distribution of the O–C–O angle in CO_3^{2-} is also shown. The distributions are normalized by dividing by sin θ. Inset: natural logarithm of distribution of the O–C–O angle in CO_2 during intervals in which it is present in the $CaCO_3$ melt (green diamonds), and comparison with its behaviour in the gas phase (black circles); see Methods. Parabolic fits of the form $A(\theta - 180°)^2 + B$ are shown as blue and red solid lines for the $CaCO_3$ and gas-phase cases, respectively. Values of the parameters extracted: $A = -0.0025$, $B = -1.25$ ($CaCO_3$) and $A = -0.0059$, $B = -0.42$ (gas).

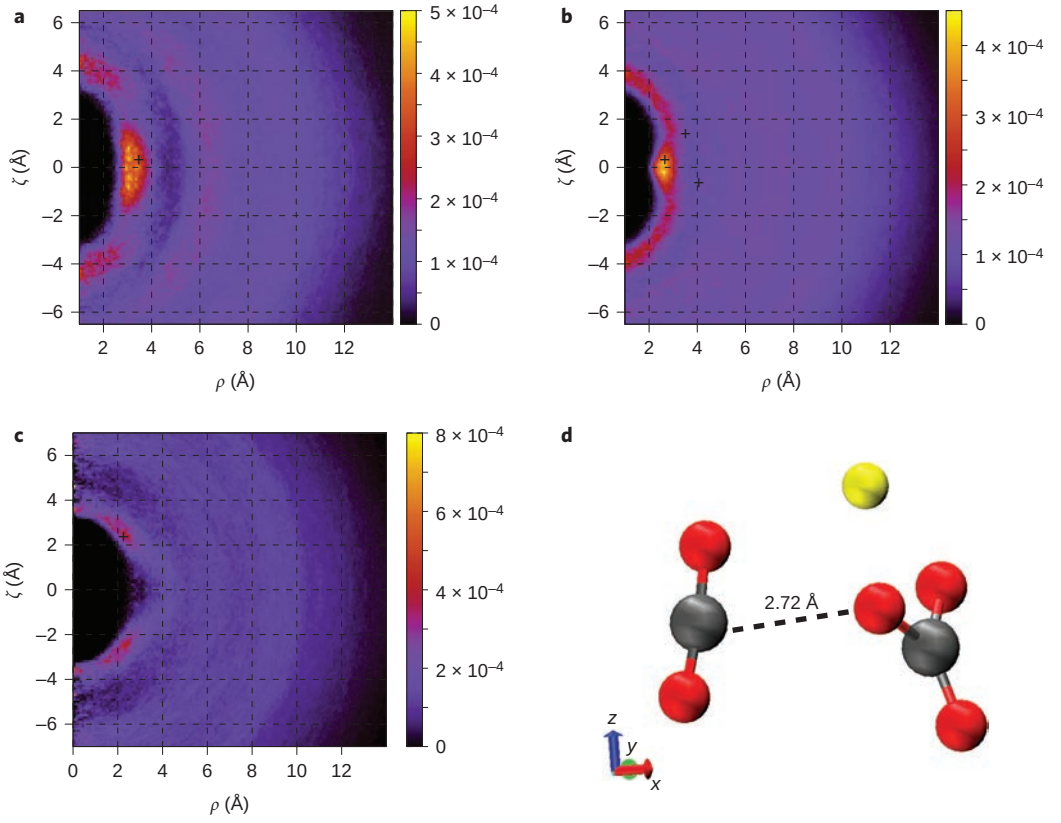

Figure 4 | Solvation structure around the CO_2 molecule. a–c, Two-dimensional colour charts (see Methods) representing the probability of the presence of the following atoms around the CO_2 molecule: C atoms (**a**); O atoms (**b**); and Ca atoms (**c**). The CO_2 molecule is oriented with its O–O axis along the $\hat{\zeta}$ direction, where $\zeta = 0$ is the mid-point of the O–O distance. ζ is thus the projection of an atom position along the O–O axis, and ρ is its distance from the O–O axis. **d**, Gas-phase geometry obtained for a cluster composed of CO_2, CO_3^{2-} and Ca^{2+} (see Methods). Cartesian axes are shown at the bottom. C, grey; O, red; Ca, yellow. Positions of the atoms of carbonate and Ca in the gas phase are marked as + symbols in the respective plots for the condensed phase. Distances are measured in ångstroms.

ionic melts. In contrast, the central C–O*–C angle is much more bent in the condensed phase than in the gas phase, by ~20°. Correspondingly, a smaller C–C distance is found in the condensed phase. We attribute the bending of the pyrocarbonate ion to charge screening occurring in the condensed phase—the charge in the pyrocarbonate ion is mainly carried by the external O atoms, while the central O* is mainly neutral (see, for example, the O–Ca RDFs shown in Supplementary Fig. 2). Charge screening by the surrounding cations therefore allows the charged molecular ends to approach closer to one another than in the gas phase. However, the O–C–O angle and consequently the O–C–O* angle remain quite similar to the gas phase case. To conclude the geometrical analysis of the pyrocarbonate ion, we calculated the O–C–O*–C dihedral angle, shown in Supplementary Fig. 3. We find that the relative orientation in the molecule is rather disordered, probably due to the transients of formation of the pyrocarbonate molecule out of CO_2 and the carbonate ion. However, a preference for periplanar configurations can be observed.

Solvation of molecular CO_2. Not only does CO_2 form $C_2O_5^{2-}$, but even in its molecular state it exhibits specific interactions with CO_3^{2-}. To characterize the solvation structure of molecular CO_2, we built two-dimensional histograms of the structure around the CO_2 molecule (see Methods for details). Figure 4a–c shows these probability density maps for C, O and Ca atoms, respectively. To facilitate the visualization and improve the statistics, we neglected the instantaneous bending of the CO_2 molecule and we built the probability histograms in a cylindrical ρ–ζ coordinate system, where the $\hat{\zeta}$ direction coincides with the O–O unit vector and ρ is the distance from the $\hat{\zeta}$ axis. The zero of the coordinate system was taken at the mid-point of the O–O vector, that is, the average position of the C atom.

Looking at Fig. 4a,b, we note the existence of a preferred position for solvation by CO_3^{2-} in the central area of the ρ–ζ representation. In fact, the largest intensities for the C atoms are observed in the region 2.75 Å $< \rho <$ 3.90 Å and −1.85 Å $< \zeta <$ 1.85 Å. For O atoms, there is instead a bright spot in the area 2.25 Å $< \rho <$ 3.00 Å and −0.55 Å $< \zeta <$ 0.55 Å. Supplementary Fig. 4 presents a histogram of the number of O atoms found in the brightest region evidenced by Fig. 4b. The probability of having at least one O in that region is ~90%. When the central ovoid red area is considered, the probability of having more than three O, and thus more than one carbonate, is close to 80%. This shows that the CO_2 molecule is closely approached by carbonate anions on a preferred pathway, eventually leading to the formation of pyrocarbonate—similar to what has been observed for CO_2 in imidazolium acetates[20]. To obtain a clearer idea of the relative orientation of CO_2 and carbonate in this precursor arrangement, we performed a gas-phase geometry optimization on a cluster composed of CO_2, CO_3^{2-} and Ca^{2+} (see Methods). The resulting geometry is shown in Fig. 4d. We find that one O of the carbonate points directly to the C of CO_2 with a C_{CO_2}–$O_{carb.}$–$C_{carb.}$ angle of ~108°. The distances found in the gas phase are compatible with the two-dimensional colour chart of Fig. 4b, although in the condensed phase the C_{CO_2}–$O_{carb.}$–$C_{carb.}$ angle is closer to ~90°. In addition to this structural analysis, Supplementary Fig. 5 presents a view of the electronic state of the molecules during the formation of the pyrocarbonate, by looking at the centres of the maximally localized Wannier functions.

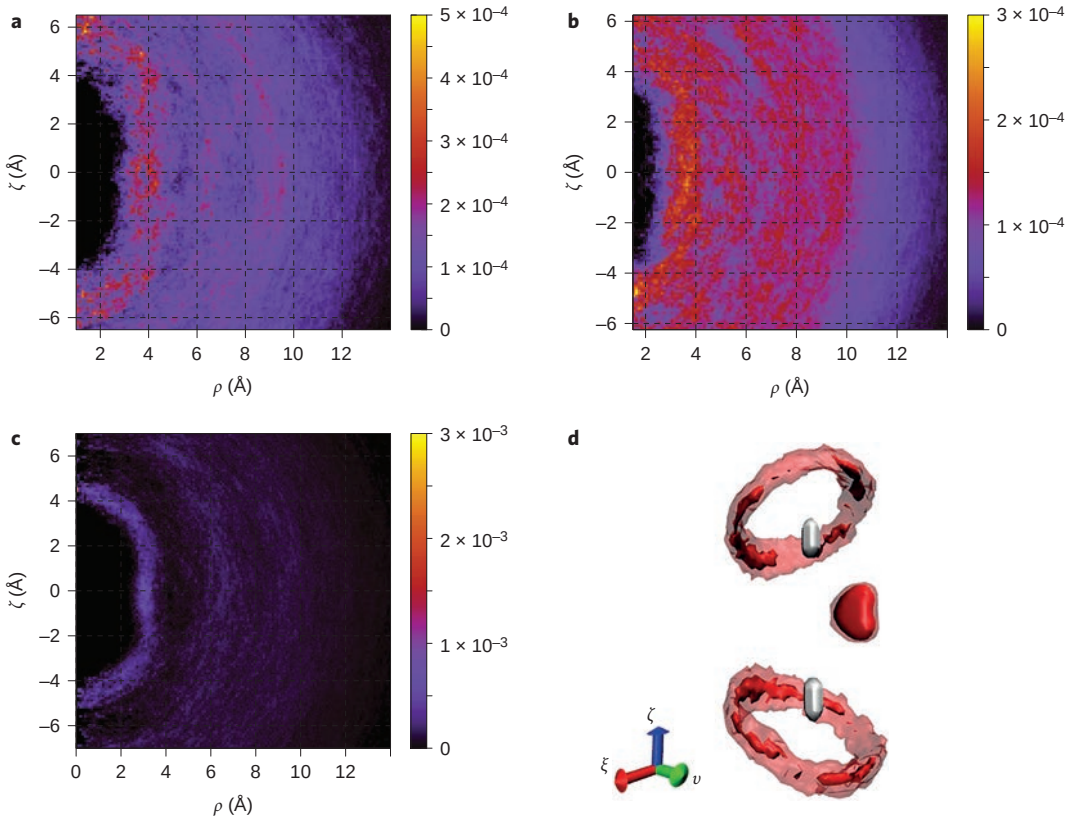

Figure 5 | Solvation structure around the pyrocarbonate ion. a–c, Two-dimensional colour charts (see Methods) representing the probability of the presence of the following atoms around the pyrocarbonate molecule: C atoms (**a**); O atoms (**b**); and Ca atoms (**c**). The $C_2O_5^{2-}$ molecule is oriented with its C–C axis along the $\hat{\zeta}$ direction, where $\zeta = 0$ is the mid-point of the C–C vector. ζ is thus the projection of an atom position along the C–C axis, and ρ is its distance from the C–C axis. The former C of the CO_2 molecule is always placed in the negative ζ portion of the plots. **d**, Three-dimensional density maps of the pyrocarbonate molecule (see Methods). The $\hat{\zeta}$ direction coincides with the C–C axis, the $\hat{\upsilon}$ direction is the perpendicular to $\hat{\zeta}$ passing by O* and $\hat{\xi} = \hat{\upsilon} \times \hat{\zeta}$. Iso-probability surfaces are plotted corresponding to $P = 0.005$ for C (grey), $P = 0.002$ for O (transparent red) and $P = 0.007$ for O (solid red). Distances are measured in ångstroms.

In Fig. 4d, a large excluded volume region is present for Ca atoms around the CO_2 molecule. Interestingly, in the region corresponding to the brightest spot for C and O, a dark spot is visible for Ca. However, Ca does seem to play a role in the approach of carbonate to CO_2. In fact, the position of Ca found in the gas phase (Fig. 4d) corresponds to the intense region just outside the excluded volume. Small bright spots are also visible at $\rho \simeq 0$ and at distances (along $\hat{\zeta}$) three to four times the C–O distance (~1.17 Å), where carbonate ions are already interposed to screen the Ca^{2+} charge.

Pyrocarbonate solvation. In contrast to the case of molecular CO_2, the solvation structure of pyrocarbonate is more diffuse. Given the mostly periplanar symmetry indicated by the dihedral angle (Supplementary Fig. 3), we continue to neglect one dimension and produce two-dimensional histograms, analogous to what is shown in Fig. 4 for the CO_2 molecule. In this case, the vertical $\hat{\zeta}$ axis coincides with the C–C direction, and ρ is the distance from this axis. The centre of the coordinate system is taken at the mid-point of the C–C vector (see Methods). We also keep track of the C atom that is part of the CO_2 molecule before the formation of the pyrocarbonate, and the charts are constructed in such a way that the C formerly belonging to CO_2 is always found at the bottom of the plots.

Figure 5a presents two-dimensional histograms for the C atoms around the pyrocarbonate. The solvation of pyrocarbonate by C atoms is almost uniform, with a small dent in the central region around $\zeta \simeq 0$ and $\rho \simeq 3$ corresponding to a modest electrostatic attraction by the central O* atom of pyrocarbonate and repulsion by the two C atoms. In addition, we observe three consecutive solvation shells, with the first being the most intense. Figure 5b shows the equivalent two-dimensional histogram for O atoms. Given that O is attached to C in carbonate ion units, the positions of the O atoms follows from that of the C, although we see here that the situation for the O appears much more diffuse, corresponding to a random orientation of the plane of the carbonate molecules in the liquid phase. One small bright spot is visible at $\zeta \simeq -4.5$ and $\rho \simeq 0$. Because the C formerly in CO_2 is, by construction, always found in the negative ζ portion, this possibly indicates that another CO_3^{2-} was or is in competition for the formation of pyrocarbonate. This is compatible with Supplementary Fig. 4, where we see that the most intense spots in Fig. 4b correspond to one or two carbonate molecules close to CO_2.

Figure 5c shows the two-dimensional histogram for Ca atoms. As in the case of C atoms, we observe an almost uniform first solvation shell with a central dent, corresponding to attraction by the O* atom and repulsion by the C atoms of pyrocarbonate. Furthermore, we notice a small bright spot at $\rho \simeq 0$, $\zeta \simeq 4.5$, probably corresponding to the fact that Ca is close to the previous CO_3^{2-} unit, rather than to the previous CO_2. Finally, Fig. 5d plots the three-dimensional isoprobability surfaces for the atoms composing the pyrocarbonate, derived from three-dimensional histograms calculated as described in the Methods. The plot shows how the position of the O in pyrocarbonate is orientationally disordered in the condensed phase, probably due to the transients of formation/dissociation. When the isoprobability value is increased, distinct spots appear that are consistent with periplanar configurations, $0° < \varphi < 30°$ or $150° < \varphi < 180°$, and with configurations with the two pairs of external O nearly perpendicular to each other, $80° < \varphi < 110°$ (Supplementary Fig. 3).

Conclusions

In summary, our study of CO_2 solvation in molten calcium carbonate by FPMD confirms the presence of the pyrocarbonate anion and of the equilibrium $CO_2 + CO_3^{2-} \rightleftharpoons C_2O_5^{2-} \rightleftharpoons CO_3^{2-} + CO_2$. We have observed how the transport of CO_2 in molten carbonate occurs in a manner similar to the Grotthuss mechanism in water, and we term this the 'oxo-Grotthuss mechanism'. We have characterized the geometry of pyrocarbonate and found it has a periplanar configuration, with the central C–O*–C bridge much more bent than in the gas phase, due to charge screening by the counterions. Furthermore, we have observed that the interaction between CO_2 and CO_3^{2-} leading to the formation of pyrocarbonate occurs along a preferred pathway, with the carbonate ion approaching CO_2 'laterally'. The enhanced transport of CO_2 by O^{2-} exchange—three times faster than molecular diffusion—may also explain the diffusivity of CO_2 in mixed oxide–carbonate materials[15].

The CO_2/CO_3^{2-} equilibrium can also be described in the framework of oxo-acidity, with CO_2 being the acid and CO_3^{2-} its conjugated base. In this context, Grotthuss-like transport may be rather general when an acid is dissolved in its conjugated base.

Methods

FPMD simulations. We have studied a system originally composed of 127 CO_3^{2-} carbonate anions, 127 Ca^{2+} calcium cations and one CO_2 molecule (638 atoms, 4,080 valence electrons). We fixed the side of the cubic simulation box to be $L = 20.054$ Å, which gives a density of $\rho = 2.63$ g cm^{-3}. The CO_2 concentration is thus 0.206 mol l^{-1}, a value typical for alkali molten salts under 1 atm of CO_2[21]. We set the temperature, controlled by the Nosé–Hoover thermostat chain[22,23] with a time constant $\tau = 0.5$ ps, at $T = 1{,}773$ K. This thermodynamic point is located, according to the pure $CaCO_3$ melting curve obtained by Suito *et al.*[24] and Spivak *et al.*[25], along the melting curve of disordered pure calcite (no CO_2).

We performed FPMD simulations based on DFT and the Born–Oppenheimer dynamics, and used the software CP2K (ref. 26) and in particular the Quickstep algorithm[27]. The latter employs a hybrid Gaussian plane-wave method (GPW)[28]. The Goedecker–Teter–Hutter (GTH) norm-conserving pseudo-potentials[29–31] were used to replace the core electrons. We cut off the electronic density at 400 Ry and used NN50 smoothing to apply the exchange–correlation potential. For C and O atoms, a triple-zeta valence doubly polarized (TZV2P) basis set was used[32], and for Ca atoms we used a double-zeta valence plus polarization (DZVP) basis set optimized for molecules[33]. The exchange–correlation interactions were taken into account by the gradient-corrected BLYP functional[34,35]. Dispersive interactions corrections were added by using the DFT-D2 scheme[36], with a cutoff of 40 Å.

The starting configuration was taken from previous equilibrated FPMD simulations of pure liquid $CaCO_3$ (128 units)[17] after having replaced one CO_3^{2-} with CO_2 and having erased one Ca^{2+} from the simulation box. We ran the simulation in the canonical *NVT* ensemble, with the simulation time step set to 0.5 fs and periodic boundary conditions. The trajectory at every time step was stored for post–run–time analysis. We accumulated the trajectory for ~65 ps (130,000 simulation steps).

In addition, we also performed a FPMD simulation of CO_2 in the gas phase, as well as geometry optimizations of the pyrocarbonate ion in the gas phase and a cluster composed of CO_2, CO_3^{2-} and Ca^{2+} (shown in Fig. 4d). Details for these can be found in Supplementary Section 'Methods'.

Analysis. Analysis of the simulation trajectory was performed using an in-house analysis suite. To define molecules from the atomic positions at each time step, we used a depth first search (DFS) closure algorithm[37]. A particular 'hysteresis' criterion was applied to define whether, in a given time frame, there was molecular CO_2 or a pyrocarbonate ion. If molecular CO_2 was in the previous time frame, we accounted for the formation of the pyrocarbonate in the current frame only when the C–O* distance was less than 1.7 Å. On the other hand, if we had pyrocarbonate in the previous frame, we accounted for a dissociation event in the current frame only when the C–O* distance became larger than 1.95 Å. This criterion allowed smoothing of the behaviour observed when a simple distance cutoff criterion is used, and was inspired by the criteria used for correlations in hydrogen bond dynamics in water[38].

To build the two-dimensional colour charts around the CO_2 molecules (Fig. 4), the coordinates were first recentred, with the centre $\mathbf{r}_c$ defined as the mid-point of the CO_2 O–O vector. We defined the $\hat{\zeta}$ direction as the O–O unit vector, and then calculated the coordinate ζ of a given atom as $\zeta = \mathbf{r}'_i \cdot \hat{\boldsymbol{\zeta}}$, where $\mathbf{r}'_i = \mathbf{r}_i - \mathbf{r}_c$. Coordinate ρ is given by $\rho = \sqrt{||\mathbf{r}'_i||^2 - \zeta^2}$ or equivalently by $\rho = ||\mathbf{r}'_i - \zeta\hat{\boldsymbol{\zeta}}||$. We binned the space by $\Delta\zeta = \Delta\rho = 0.1$ Å in the intervals between $-L/2$ and $L/2$ for ζ and 0 and $\sqrt{2}L/2$ for ρ. The two-dimensional intensity histogram was normalized by dividing by the product of the number of steps, by the number of particles of type α (α = C, O, Ca) and by the bin volume $2\pi\rho\Delta\rho\Delta\zeta$.

For construction of the two-dimensional colour charts around the pyrocarbonate ion (Fig. 5), we followed an analogous procedure, with the only difference being that the C–C direction was now taken as $\hat{\zeta}$ and the mid-point of the C–C vector as centre. Furthermore, we specifically took the beginning of the C–C vector corresponding to the C atom that was part of the CO_2 molecule just before the formation of the pyrocarbanate ion. The former C of the CO_2 molecule was thus always found in the negative ζ portion of the plots.

We also built three dimensional density maps for C and O (for example, Fig. 5d). In those plots, axis $\hat{\zeta}$ coincides with the C–C direction, the $\hat{v}$ axis is obtained from CO*–(CO*·$\hat{\zeta}$)$\hat{\zeta}$ and $\hat{\xi} = \hat{v} \times \hat{\zeta}$. We recentred the coordinates around the mid-point of the C–C vector $\mathbf{r}_c$, $\mathbf{r}'_i = \mathbf{r}_i - \mathbf{r}_c$. The new coordinates were thus $\xi = \mathbf{r}'_i \cdot \hat{\boldsymbol{\xi}}$, $v = \mathbf{r}'_i \cdot \hat{\boldsymbol{v}}$ and $\zeta = \mathbf{r}'_i \cdot \hat{\boldsymbol{\zeta}}$. We binned the space by $\Delta\xi = \Delta v = \Delta\zeta = 0.1$ Å between –6.0 and 6.0 Å. The intensity histograms were normalized by dividing by the number of steps, the number of particles of type α (α = C, O, Ca) and by the volume of the bin $\Delta\xi\Delta v\Delta\zeta$. Molecular representations and iso-probability surfaces were visualized using the software VMD[39].

Received 26 July 2015; accepted 7 January 2016; published online 29 February 2016

References

1. Gaillard, F., Malki, M., Iacono-Marziano, G., Pichavant, M. & Scaillet, B. Carbonatite melts and electrical conductivity in the asthenosphere. *Science* **322,** 1363–1365 (2008).
2. Jones, A. P., Genge, M. & Carmody, L. Carbonate melts and carbonatites. *Rev. Mineral. Geochem.* **75,** 289–322 (2013).
3. Kaminsky, F., Wirth, R., Schreiber, A. & Thomas, R. Nyerereite and nahcolite inclusions in diamond: evidence for lower-mantle carbonatitic melts. *Mineral. Mag.* **73,** 797–816 (2009).
4. Stoppa, F., Jones, A. P. & Sharygin, V. Nyerereite from carbonatite rocks at Vulture volcano: implications for mantle metasomatism and petrogenesis of alkali carbonate melts. *Cent. Euro. J. Geosci.* **1,** 131–151 (2009).
5. Kaminsky, F. Mineralogy of the lower mantle: a review of 'super-deep' mineral inclusions in diamond. *Earth Sci. Rev.* **110,** 127–147 (2012).
6. Dasgupta, R. & Hirschmann, M. M. The deep carbon cycle and melting in Earth's interior. *Earth Planet. Sci. Lett.* **298,** 1–13 (2010).
7. Dasgupta, R. & Hirschmann, M. M. Melting in Earth's deep upper mantle caused by carbon dioxide. *Nature* **440,** 659–662 (2006).
8. Chery, D., Lair, V. & Cassir, M. CO_2 electrochemical reduction into CO or C in molten carbonates: a thermodynamic point of view. *Electrochim. Acta* **160,** 74–81 (2015).
9. Chery, D., Albin, V., Lair, V. & Cassir, M. Thermodynamic and experimental approach of electrochemical reduction of CO_2 in molten carbonates. *Int. J. Hydrogen Energy* **39,** 12330–12339 (2014).
10. Kanai, Y., Fukunaga, K., Terasaka, K. & Fujioka, S. Mass transfer in molten salt and suspended molten salt in bubble column. *Chem. Eng. Sci.* **100,** 153–159 (2013).
11. Claes, P., Moyaux, D. & Peeters, D. Solubility and solvation of carbon dioxide in the molten $Li_2CO_3/Na_2CO_3/K_2CO_3$ (43.5:31.5:25.0 mol-%) eutectic mixture at 973K. I. Experimental part. *Eur. J. Inorg. Chem.* **1999,** 583–588 (1999).
12. Peeters, D., Moyaux, D. & Claes, P. Solubility and solvation of carbon dioxide in the molten $Li_2CO_3/Na_2CO_3/K_2CO_3$ (43.5:31.5:25.0 mol-%) eutectic mixture at 973K. II. Theoretical part. *Eur. J. Inorg. Chem.* **1999,** 589–592 (1999).
13. Burna, P. J., Grein, F. & Passmore, J. Density functional theory (DFT) calculations on the structures and stabilities of $[C_nO_{2n+1}]^{2-}$ and $[C_nO_{2n+1}]X_2$ polycarbonates containing chainlike $(CO_2)_n$ units (n=2–6; X=H or Li). *Can. J. Chem.* **89,** 671–687 (2011).
14. Frapper, G. & Saillard, J.-Y. Search for new allotropic forms of carbon dioxide and carbon disulfide: a density functional study of CX_2-based oligomers (X= O, S). *J. Am. Chem. Soc.* **122,** 5367–5370 (2000).
15. Zhang, L. *et al.* First spectroscopic identification of pyrocarbonate for high CO_2 flux membranes containing highly interconnected three dimensional ionic channels. *Phys. Chem. Chem. Phys.* **15,** 13147–13152 (2013).
16. Zeller, K.-P., Schuler, P. & Haiss, P. The hidden equilibrium in aqueous sodium carbonate solutions—evidence for the formation of the dicarbonate anion. *Eur. J. Inorg. Chem.* 168–172 (2005).
17. Vuilleumier, R., Seitsonen, A., Sator, N. & Guillot, B. Structure, equation of state and transport properties of molten calcium carbonate ($CaCO_3$) by atomistic simulations. *Geochim. Cosmochim. Acta.* **141,** 547–566 (2014).
18. Vuilleumier, R., Seitsonen, A. P., Sator, N. & Guillot, B. Carbon dioxide in silicate melts at upper mantle conditions: insights from atomistic simulations. *Chem. Geol.* **418,** 77–88 (2015).
19. Saitta, A. M., Saija, F. & Giaquinta, P. V. *Ab initio* molecular dynamics study of dissociation of water under an electric field. *Phys. Rev. Lett.* **108,** 207801 (2012).
20. Kelemen, Z. *et al.* An abnormal N-heterocyclic carbene–carbon dioxide adduct from imidazolium acetate ionic liquids: the importance of basicity. *Chem. Eur. J.* **20,** 13002–13008 (2014).
21. Chery, D., Lair, V. & Cassir, M. Overview on CO_2 valorization: challenge of molten carbonates. *Front. Energy Res.* **3,** 43 (2015).
22. Nosé, S. A molecular-dynamics method for simulations in the canonical ensemble. *Mol. Phys.* **52,** 255–268 (1984).

23. Nosé, S. A unified formulation of the constant temperature molecular-dynamics methods. *J. Chem. Phys.* **81,** 511–519 (1984).
24. Suito, K. *et al.* Phase relations of $CaCO_3$ at high pressure and high temperature. *Am. Mineral.* **86,** 997–1002 (2001).
25. Spivak, A. V., Litvin, Y. A., Ovsyannikov, S. V., Dubrovinskaia, N. A. & Dubrovinsky, L. S. Stability and breakdown of $Ca^{13}CO_3$ melt associated with formation of ^{13}C-diamond in static high pressure experiments up to 43 GPa and 3900 K. *Solid State Chem.* **191,** 102–106 (2012).
26. Hutter, J., Iannuzzi, M., Schiffmann, F. & VandeVondele, J. CP2K: atomistic simulations of condensed matter systems. *WIREs Comput. Mol. Sci.* **4,** 15–25 (2014).
27. VandeVondele, J. *et al.* QUICKSTEP: fast and accurate density functional calculations using a mixed Gaussian and plane waves. *Comp. Phys. Commun.* **167,** 103–128 (2005).
28. Lippert, G., Hutter, J. & Parrinello, M. A hybrid Gaussian and plane wave density functional scheme. *Mol. Phys.* **92,** 477–487 (1997).
29. Goedecker, S., Teter, M. & Hutter, J. Separable dual-space Gaussian pseudopotentials. *Phys. Rev. B* **54,** 1703–1710 (1996).
30. Hartwigsen, C., Goedecker, S. & Hutter, J. Relativistic separable dual-space Gaussian pseudopotentials from H to Rn. *Phys. Rev. B* **58,** 3641–3662 (1998).
31. Krack, M. Pseudopotentials for H to Kr optimized for gradient-corrected exchange-correlation functionals. *Theor. Chem. Acc.* **114,** 145–152 (2005).
32. VandeVondele, J. *et al.* The influence of temperature and density functional models in *ab initio* molecular dynamics simulation of liquid water. *J. Chem. Phys.* **122,** 014515 (2005).
33. VandeVondele, J. & Hutter, J. Gaussian basis sets for accurate calculations on molecular systems in gas and condensed phases. *J. Chem. Phys.* **127,** 114105 (2007).
34. Becke, A. D. Density-functional exchange-energy approximation with correct asymptotic behavior. *Phys. Rev. A* **38,** 3098–3100 (1988).
35. Lee, C., Yang, W. & Parr, R. G. Development of the Colle–Salvetti correlation energy formula into a functional of the electron density. *Phys. Rev. B* **37,** 785–789 (1988).
36. Grimme, S. Semiempirical GGA-type density functional constructed with a long-range dispersion correction. *J. Comput. Chem.* **27,** 1787–1799 (2006).
37. Cormen, T. H., Leiserson, C. E., Rivest, R. L. & Stein, C. *Introduction to Algorithms* (MIT Press, 1990).
38. Laage, D. & Hynes, J. T. A molecular jump mechanism of water reorientation. *Science* **311,** 832–835 (2006).
39. Humphrey, W., Dalke, A. & Schulten, K. VMD—visual molecular dynamics. *J. Mol. Graph.* **14,** 33–38 (1996).

Acknowledgements

The authors thank M. Cassir, V. Lair, B. Guillot, F. Gaillard, V. Haigis and A. Boutin for discussions. The research reported herein was funded by PSL Research University (project COOCAR, grant ANR-10-IDEX-0001-02) and Agence Nationale de la Recherche (project ELECTROLITH, grant ANR-2010-BLAN-621-03). This work was performed using HPC resources from GENCI (grants 2013-082309, 2014-082309 and 2015-082309) and IDRIS (grant 'Grand Challenge' 100577). The authors acknowledge PRACE for awarding access to Resource Curie, based in France at CEA Bruyères-le-Chatel (preparatory access allocation 2010PA2746).

Author contributions

R.V. performed the FPMD simulations. D.C. analysed the trajectories, prepared the figures and wrote the manuscript. All authors designed the research, discussed the results and revised the manuscript.

Additional information

Supplementary information is available in the online version of the paper. Reprints and permissions information is available online at www.nature.com/reprints. Correspondence and requests for materials should be addressed to F.X.C. and R.V.

Competing financial interests

The authors declare no competing financial interests.

Braiding Majorana zero modes using quantum dots

Corneliu Malciu,[1] Leonardo Mazza,[2] and Christophe Mora[1]

[1] *Laboratoire Pierre Aigrain, École Normale Supérieure-PSL Research University, CNRS, Université Pierre et Marie Curie-Sorbonne Universités, Université Paris Diderot-Sorbonne Paris Cité, 24 rue Lhomond, 75231 Paris Cedex 05, France*

[2] *Département de physique, École Normale Supérieure-PSL Research University, CNRS, 24 rue Lhomond, 75231 Paris Cedex 05, France*

(Dated: May 25, 2018)

We discuss a network of Kitaev wires coupled to several individually-tunable quantum dots as an extension of the recent experiments on a quantum dot coupled to a nanowire hosting Majorana zero modes [Deng et al. Science **354** 1557 (2016) and Deng et al. arXiv:1712.03536 (2017)]. The setup features localized Majorana modes with exact zero energy and we show that they can be manipulated by solely acting on the quantum dots. A braiding process can be obtained by arranging three wires as a trijunction and a charge readout of the quantum dots can be used to reveal the non-Abelian statistics of Majorana zero modes. The setup can be scaled up to serve the more advanced purposes of topological quantum computation.

I. INTRODUCTION

After their introduction in 1937 in the context of the relativistic Dirac equation[1], Majorana fermions have recently experienced a renewed interest for their relevance in the description of some low-dimensional and superconducting topological models[2–9]. In this context, they typically bind to defects (e.g. vortices in the p+ip model[10]) or to boundaries between topological and non-topological phases (e.g. at the edges of Kitaev's chain[11]); they are zero-energy modes whose appearance is topologically protected from small perturbations. Remarkably, Majorana zero modes (MZM) exhibit an exchange statistics that is neither bosonic nor fermionic: they are non-Abelian anyons and as such they imply a degeneracy of the many-body ground state[12].

The topological protection of MZMs gave them a very special status: they lie at the heart of current proposals for hardware-based fault-tolerant quantum computation[13–23]. Their non-Abelian statistics can be used to perform non-trivial operations on the ground states through the adiabatic exchange of two anyon positions, which is described by their braiding group[24–36]. Since it is not sufficient for performing universal quantum computation, it has been suggested that projective measurements could be used to implement the missing gates[37–39].

There have been important experimental progresses in the recent years regarding the realization and observation of MZMs in solid-state devices. The community has focused on hybrid semiconductor-superconductor setups[40–52] and chains of magnetic adatoms coupled to conventional superconductors[53–59]. The recent proposals for MZMs in two-dimensional electron gases proximitized to superconductors promise a new generation of platforms significantly less affected by disorder[60,61]. Yet, discerning MZMs from the variety of phenomena producing sub-gap states is still an experimental challenge[62,63].

In order to distinguish topological and trivial excitations without performing braiding, it has been suggested that a quantum dot (QD) could be used as a probe of the non-locality of MZM[64–70]. The key idea is to alter the zero-bias conductance measurements by adding a tunable QD between the lead and the wire: the entire conductance pattern observed as the dot is tuned through resonance provides information about topological properties. The successful experimental realization of such a device and the characterization of the non-local nature of the zero-energy excitation[50,51] demonstrate that nanowires coupled to QDs are an experimentally practical and promising route for the study and exploit of electronic liquids supporting Majorana zero modes.

In this work, we show that such experimental setups can also be employed for performing braiding operations. We demonstrate this by studying a network of Kitaev wires, each one connected to one or more QDs, and show that they host exact MZMs that can be controlled and transported at will by only manipulating the QDs. Additionally, the QDs serve the purpose of parity readout[71], which is necessary for obtaining the experimental confirmation that the braiding process occurred. By measuring the parity of the total charge of two neighbouring QDs, and considering larger networks with a more complex structure, it is possible to scale up the system with the objective of topological quantum computation.

This article is organized as follows: in Sec. II we briefly recall some results on Kitaev's wire coupled to a QD. In Sec. III we discuss how to braid the MZMs that appear in such setup and how to measure the outcome of such operation using QDs. In Sec. IV we outline the scale-up of such protocol to the realization of topological quantum computation in QD-controlled circuits. Our conclusions are presented in Sec. V.

II. A KITAEV WIRE COUPLED TO A QUANTUM DOT

In this section we consider a tunable QD which is tunnel-coupled to the left edge of a Kitaev wire, a setup that has been theoretically studied in Ref. 64, and also in

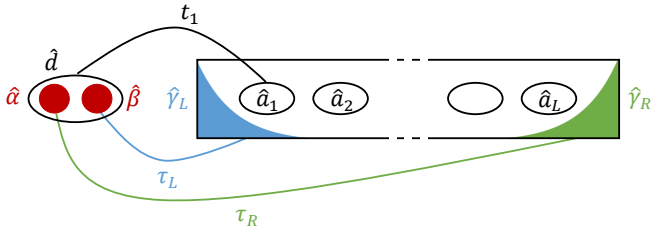

FIG. 1. Scheme of the QD-wire setup: a QD with a single fermionic mode is connected to the first site of a Kitaev wire through a real hopping amplitude t_1. The low-energy subspace is described by four Majorana modes $\hat{\alpha}$, $\hat{\beta}$ (QD) and $\hat{\gamma}_L$, $\hat{\gamma}_R$ (wire, exponentially localized at the edges). The effective couplings $\tau_{L,R}$ between the QD and the wire are defined in Eq. (2) and shown in the figure.

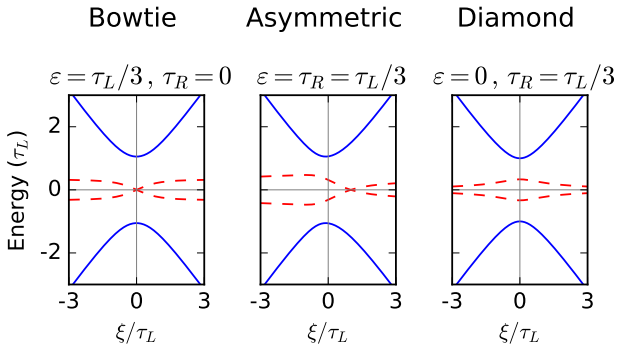

FIG. 2. The *bowtie*, *asymmetric* and *diamond* patterns observed in the model (2) when the QD energy ξ crosses zero. Far from $\xi = 0$, the linear dispersion (solid blue) corresponds to the QD energies, and the split levels (dashed red) correspond to the $\hat{\gamma}_{L,R}$ of the wire. The patterns are observed both with the effective model (plotted here) and with the full microscopic Hamiltonian (1) (not shown). Assuming $|\tau_R| \ll |\tau_L|$, couplings are extracted as follows: ε is the energy splitting of the Majorana $\hat{\gamma}_{L,R}$ far from resonance, $2|\tau_L|$ is the minimum gap between the solid blue lines, the position of this minimum sets the origin for ξ, and finally τ_R is obtained from the zero-energy crossing predicted by Eq. (3).

the more experimentally-relevant spinful case in Ref. 65. We briefly review some of their results and stress that thanks to the tunability of the QD it is always possible to have Majorana modes with exactly zero energy.

A. Effective model

We model the QD with a single fermionic mode using canonical operators $\hat{d}^{(\dagger)}$; the Kitaev wire has length L and its fermionic modes are described by the operators $\hat{a}_j^{(\dagger)}$, $j = 1 \dots L$. The full Hamiltonian reads (see Fig. 1):

$$\hat{H}_{\text{QD-K}} = e_d\, \hat{d}^\dagger \hat{d} - t_1 \left(\hat{d}^\dagger \hat{a}_1 + \hat{a}_1^\dagger \hat{d} \right) + \hat{H}_K; \tag{1}$$

$$\hat{H}_K = \sum_{j=1}^{L} \left\{ \left(-t \hat{a}_j^\dagger \hat{a}_{j+1} - \Delta \hat{a}_j \hat{a}_{j+1} + \text{h.c.} \right) - \mu\, \hat{a}_j^\dagger \hat{a}_j \right\};$$

where e_d is the tunable energy of the QD, t is the hopping term of the wire, $\Delta = |\Delta| e^{i\phi}$ its pairing term and μ its chemical potential. Without loss of generality t_1 is taken real. For $|\mu| < 2t$ and $\Delta \neq 0$, Hamiltonian $\hat{H}_K$ exhibits topological subgap states, which are Majorana modes exponentially localized at the left and right edges of the wire, $\hat{\gamma}_L$ and $\hat{\gamma}_R$; for a finite length L, they have an exponentially-small energy $\varepsilon \sim e^{-L}$. We assume to be in this topological phase.

In order to capture the low-energy behaviour of the full system, it is sufficient to consider the coupling of the QD to the edge states of the wire. We perform a gauge transformation on the $\hat{d}^{(\dagger)}$ so that, by decomposing it into two Majorana fermions $\hat{\alpha} = \hat{d} + \hat{d}^\dagger, \hat{\beta} = -i(\hat{d} - \hat{d}^\dagger)$, we get (see the sketch in Fig. 1):

$$\hat{H}^{\text{eff}}_{\text{QD-K}} = i \left(\xi\, \hat{\alpha}\hat{\beta} + \varepsilon\, \hat{\gamma}_L \hat{\gamma}_R + \tau_L\, \hat{\beta}\hat{\gamma}_L + \tau_R \hat{\alpha}\hat{\gamma}_R \right), \tag{2}$$

where $\xi = e_d/2$. Terms proportional to the identity have been omitted and the expression is particularly simple because Hamiltonian (1) is unitarily related to a time-reversal invariant one. The effective couplings τ_L and τ_R depend on the projection of $\hat{\gamma}_L$ and $\hat{\gamma}_R$ on the first site $\hat{a}_1$ of the wire, and can be chosen real; clearly, $\tau_R \sim e^{-L}$. Because this Hamiltonian describes the sub-gap physics, we implicitly assumed $\xi, \tau_L, \tau_R, \varepsilon \ll E_G$, where $E_G \sim |\Delta|$ is the energy gap of the many-body system.

Three different patterns, dubbed *bowtie* ($\varepsilon \neq 0, \tau_R = 0$), *asymmetric* ($\varepsilon \neq 0, \tau_R \neq 0$), and *diamond* ($\varepsilon = 0, \tau_R \neq 0$) can be observed and are shown in Fig. 2. They exhibit a zero-energy crossing, indicating a parity switch of the many-body ground state, occurring exactly at (see Appendix A):

$$\xi_c = -\frac{\tau_L \tau_R}{\varepsilon}. \tag{3}$$

For the fine-tuned *diamond* case where the energy splitting ε between the two Majorana bound states vanishes, $|\xi_c| \to \infty$. All three patterns can be recovered from the microscopic Hamiltonian in Eq. (1). The effective couplings used in Eq. (2) can be extracted through spectroscopic (non-linear conductance) measurements as recently observed by Deng et al.[50,51].

The parity switch of the ground state occurring at ξ_c can be understood in terms of charge transport from the dot to the wire. As ξ is adiabatically tuned from $-\infty$ to $+\infty$ during a period T (sent to $+\infty$ for a truly adiabatic evolution), the QD which was initially charged unloads into the wire. At $t = 0$ and $t = T$ the dot and the wire are effectively uncoupled, and both subsystems have a

definite parity:

$$\begin{aligned} t=0 \ : \quad & \hat{P}_d = i\hat{\alpha}\hat{\beta} = 1 \qquad \hat{P}_w = i\hat{\gamma}_L\hat{\gamma}_R = \chi \\ t=T \ : \quad & \hat{P}_d = -1 \qquad\qquad \hat{P}_w = -\chi \end{aligned} \tag{4}$$

where $\chi = -\mathrm{sgn}(\varepsilon)$. Because the total parity $\hat{P} = \hat{P}_d\hat{P}_w$ is conserved by the Hamiltonian, the final wire parity must be $-\chi$. This protocol adiabatically drives the system into an excited state similarly to what occurs in the 4π Josephson effect. Note, however, that $\hat{P}_w$ is reversed here, whereas it remains unchanged in the Josephson setup.

B. Exact MZMs

In the most general case, a finite Kitaev wire does not host true zero-energy states (called MZMs) since $\varepsilon \neq 0$. However, the effective model (2) is degenerate for $\xi = \xi_c$, and therefore hosts a pair of MZMs, denoted below $\hat{\gamma}_1$ and $\hat{\gamma}_2$ (MZMs always come in pairs because of the particle-hole symmetry of the Bogoliubov-de Gennes Hamiltonian). Thus, a tunnel contact to a quantum dot with a tunable orbital energy can induce genuine MZM, later needed for topologically-protected quantum operations.

In order to gain further insights on the spatial position of $\hat{\gamma}_1$ and $\hat{\gamma}_2$, we first consider the simplest case $\varepsilon = 0$ and $\tau_R = 0$, so that the Hamiltonian

$$\hat{H}^{\text{eff}}_{\text{QD-K}} = i\xi\,\hat{\alpha}\hat{\beta} + i\tau_L\,\hat{\beta}\hat{\gamma}_L, \tag{5}$$

decouples the Majorana fermion $\hat{\gamma}_R$: $\hat{\gamma}_R$ is a MZM and we arbitrarily identify it with $\hat{\gamma}_2$. The other MZM is:

$$\hat{\gamma}_1 = \frac{1}{\mathcal{N}}\left(\hat{\gamma}_L + \frac{\tau_L}{\xi}\hat{\alpha}\right), \qquad \mathcal{N} = \sqrt{1+\left(\frac{\tau_L}{\xi}\right)^2}, \tag{6}$$

whose spatial localization is controlled by the QD energy ξ; for instance $\hat{\gamma}_1 = \hat{\gamma}_L$ when $|\xi| \to \infty$ and $\hat{\gamma}_1 = \hat{\alpha}$ when $\xi = 0$. This ability to move the MZM from the wire to the QD by tuning the QD energy ξ is the key to the braiding and readout procedures presented in this article. Note also the spatial separation of $\hat{\gamma}_1$ and $\hat{\gamma}_2$.

In the general case, namely the *asymetric* configuration in Fig. 2, the effective Hamiltonian (2) exhibits two MZM at $\xi = \xi_c$ given by

$$\hat{\gamma}_1 = \frac{1}{\mathcal{N}_1}\left(\hat{\alpha} - \frac{\tau_R}{\varepsilon}\hat{\gamma}_L\right), \qquad \mathcal{N}_1 = \sqrt{1+\left(\frac{\tau_R}{\varepsilon}\right)^2}, \tag{7a}$$

$$\hat{\gamma}_2 = \frac{1}{\mathcal{N}_2}\left(\hat{\gamma}_R + \frac{\varepsilon}{\tau_L}\hat{\beta}\right), \qquad \mathcal{N}_2 = \sqrt{1+\left(\frac{\varepsilon}{\tau_L}\right)^2}. \tag{7b}$$

In the *bowtie* configuration, τ_R vanishes and thus $\xi_c = 0$. Setting the QD energy to zero $\xi = 0$ in the Hamiltonian (2) decouples $\hat{\alpha}$ and thus localizes the first MZM on the QD ($\hat{\gamma}_1 = \hat{\alpha}$); this is in agreement with Eq. (7a).

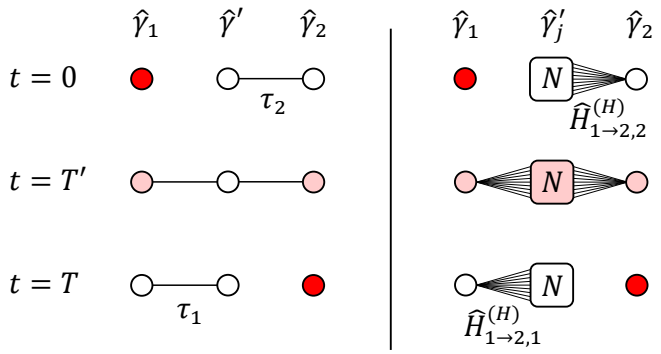

FIG. 3. *Left:* Transport of a MZM from $\hat{\gamma}_1$ to $\hat{\gamma}_2$ through $\hat{\gamma}'$ by tuning the couplings $\tau_{1,2}$. Because the total number of Majorana fermions is odd, a MZM must exist at all times. At $t = 0$, $\tau_1 = 0$ and the MZM is strictly localized on $\hat{\gamma}_1$; similarly, at $t = T$, $\tau_2 = 0$ and the MZM is strictly localized on $\hat{\gamma}_2$; at intermediary times $t = T'$, the MZM is delocalized among $\hat{\gamma}_1$ and $\hat{\gamma}_2$. Provided that the couplings are tuned adiabatically, and that the gap of the higher energy levels does not close, $\hat{\gamma}_2(T) = \pm\hat{\gamma}_1(0)$ which corresponds to the transport $1 \to 2$. *Right:* Generalization of the protocol amounting to the transport of a MZM from $\hat{\gamma}_1$ to $\hat{\gamma}_2$ through a network of N Majorana fermions $\hat{\gamma}'_j$ (N odd). Once again, the total number of Majorana fermions is odd, ensuring the existence of a MZM at all times.

For simplicity, we will set $\tau_R = 0$ in the remainder of this paper. For non-zero τ_R, the localization of the first MZM is not exactly on the QD (still it remains in the vicinity), as given by Eq. (7a), but $\xi = \xi_c$ still enforces MZMs.

III. BRAIDING MZMS WITH QDS

In this section we discuss how to braid the MZMs that we identified above. We first present a generic argument concerning the adiabatic transport of MZMs and then explicitly apply it to a trijunction where their non-Abelian statistics can be revealed through braiding.

A. Transporting Majorana fermions

We employ an argument due to Kitaev (see Sau *et al.*[26]) in order to show how topologically-protected transport of Majorana fermions can be achieved with tunable QDs. By topological protection, we mean that the final state after an adiabatic evolution is only dictated by the final and initial conditions and does not depend on the intermediate details.

We begin with a simple example by considering three Majorana fermions $\hat{\gamma}_1$, $\hat{\gamma}_2$ and $\hat{\gamma}'$ connected by time-dependent couplings:

$$\hat{H}_{1\to 2}(t) = i\tau_1(t)\hat{\gamma}_1\hat{\gamma}' + i\tau_2(t)\hat{\gamma}_2\hat{\gamma}' \tag{8}$$

and represented in Fig. 3, left panel. A fourth Majorana mode is implicitly assumed to be at zero energy, uncoupled and unperturbed during the whole time evolution. As discussed in Sec. II B, particle-hole symmetry dictates that MZMs come in pair, and therefore there is an additional MZM which is a combination of $\hat{\gamma}_1$, $\hat{\gamma}_2$ and $\hat{\gamma}'$ and the ground state is twofold degenerate at all times. The procedure starts at time $t = 0$ with $\tau_1(0) = 0$ and the MZM localized on $\hat{\gamma}_1$; it ends at time $t = T$ with $\tau_2(T) = 0$ and the MZM localized on $\hat{\gamma}_2$ (see Fig. 3, left panel). We assume that the two higher energy states are gapped out during the entire process, and that the couplings $\tau_{1,2}(t)$ are tuned adiabatically, so that the system remains in the ground state of Hamiltonian (8).

We discuss time evolution in the Heisenberg picture and use the superscript (H) for Heisenberg operators, including the Hamiltonian. Since the Hamiltonian $\hat{H}^{(H)}_{1\to 2}(t)$ and the parity operator[72] $\hat{P}^{(H)}(t) = i\hat{\gamma}_1(t)\hat{\gamma}_2(t)\hat{\gamma}'(t)$ commute at all times, it holds that $\hat{P}^{(H)}(T) = \hat{P}^{(H)}(0)$. Adiabatic evolution implies that an initial ground state $|\Psi_0\rangle$ of $\hat{H}_{1\to 2}(0)$ remains a ground state of $\hat{H}^{(H)}_{1\to 2}(t)$ at all times. Hence we have, at initial and final times,

$$\begin{aligned} i\hat{\gamma}_2\hat{\gamma}'\,|\Psi_0\rangle &= -\mathrm{sgn}[\tau_2(0)]\,|\Psi_0\rangle\,, \\ i\hat{\gamma}_1(T)\hat{\gamma}'(T)\,|\Psi_0\rangle &= -\mathrm{sgn}[\tau_1(T)]\,|\Psi_0\rangle\,. \end{aligned} \tag{9}$$

Combining this result with parity conservation, we find:

$$\hat{\gamma}_2(T)\,|\Psi_0\rangle = \pm\hat{\gamma}_1(0)\,|\Psi_0\rangle\,; \tag{10}$$

where the sign depends on the microscopic details of the Hamiltonian (here, it is $\mathrm{sgn}[-\tau_1(T)\tau_2(0)]$). Eq. (10) is interpreted as the adiabatic transport of a MZM from $\hat{\gamma}_1$ to $\hat{\gamma}_2$. Note that the same proof holds if the system is initialized in one of the two excited states $|\Psi_e\rangle$, and Eq. (10) is therefore true at the operatorial level, i.e. $\hat{\gamma}_2(T) = \pm\hat{\gamma}_1(0)$.

This scheme can be generalized to the case of the transport of a MZM from $\hat{\gamma}_1$ to $\hat{\gamma}_2$ through an arbitrary network involving an odd number of Majorana fermions $\hat{\gamma}'_j$, $j = 1 \dots N$, where N odd ensures the existence of a MZM (see Fig. 3, right panel). Again, we are implicitly assuming the existence of an additional MZM $\hat{\gamma}_0$ which never appears in the Hamiltonian but ensures an even number of Majorana modes in the system. The Hamiltonian reads:

$$\begin{aligned} \hat{H}_{1\to 2}(\{\hat{\gamma}_1,\hat{\gamma}_2,\hat{\gamma}'_j\},t) = \hat{H}_{1\to 2,1}(\{\hat{\gamma}_1,\hat{\gamma}'_j\},t) + \\ + \hat{H}_{1\to 2,2}(\{\hat{\gamma}_2,\hat{\gamma}'_j\},t) + \hat{H}_{1\to 2,3}(\{\hat{\gamma}'_j\},t). \end{aligned} \tag{11}$$

The first (second) term describes the coupling of the MZM $\hat{\gamma}_1$ ($\hat{\gamma}_2$) to the Majorana modes of the network $\{\hat{\gamma}'_j\}$. The third term is the Hamiltonian of the network. Note that none of these operators is assumed to be bilinear in the Majorana modes (they could also be quartic); however, they all conserve the total fermionic parity. Thus, $[\hat{H}^{(H)}_{1\to 2}(t), \hat{P}^{(H)}(t)] = 0$ at all times, where $\hat{P}^{(H)}(t) = \hat{\gamma}_1(t)\hat{\gamma}_2(t)\prod_j \hat{\gamma}'_j(t)$.

At $t = 0$, $\hat{H}_{1\to 2,1} = 0$ and $\hat{\gamma}_1$ is uncoupled. The two MZMs $\hat{\gamma}_0$ and $\hat{\gamma}_1$ commute with the full Hamiltonian $\hat{H}_{1\to 2}$ and thus generate the twofold degenerate ground state. We define the partial parity operator $\hat{P}_{e,1} = \hat{\gamma}_2\prod_j \hat{\gamma}'_j$ commuting with the Hamiltonian $\hat{H}_{1\to 2}$, $\hat{\gamma}_0$ and $\hat{\gamma}_1$. It follows that any ground state $|\Psi_0\rangle$ of $\hat{H}_{1\to 2}$ is an eigenstate of $\hat{P}_{e,1}$ with eigenvalue $\chi_1 = \pm 1$. The sign of χ_1 depends specifically on the microscopic details of $\hat{H}_{1\to 2}$ but remains the same within the ground state subspace. In the particular case of quadratic Hamiltonians, χ_1 is obtained by computing the sign of the Pfaffian of the matrix defined from the Majorana pairwise couplings[11]. Summarizing:

$$\hat{P}^{(H)}(0)\,|\Psi_0\rangle = \hat{\gamma}_1\hat{P}_{e,1}\,|\Psi_0\rangle = \chi_1\hat{\gamma}_1\,|\Psi_0\rangle\,. \tag{12}$$

At time $t = T$, $\hat{\gamma}_2(T)$ is uncoupled since $\hat{H}^{(H)}_{1\to 2,2}(T) = 0$. Since during the entire process there are two MZMs, the ground state remains twofold degenerate. An adiabatic evolution means that the initial ground state $|\Psi_0\rangle$ is also a ground state of $\hat{H}^{(H)}_{1\to 2}(T)$. Repeating the same arguments as for $t = 0$, we introduce the parity operator $\hat{P}^{(H)}_{e,2}(T) = \hat{\gamma}_1(T)\prod_j \hat{\gamma}'_j(T)$ commuting with the final Hamiltonian $\hat{H}^{(H)}_{1\to 2}(T)$ as well as with the MZMs $\hat{\gamma}_0(T) = \hat{\gamma}_0$ and $\hat{\gamma}_2(T)$. One obtains:

$$\hat{P}^{(H)}(T)\,|\Psi_0\rangle = -\hat{\gamma}_2(T)\hat{P}^{(H)}_{e,2}(T)\,|\Psi_0\rangle = -\chi_2\hat{\gamma}_2(T)\,|\Psi_0\rangle\,, \tag{13}$$

where χ_2 is the eigenvalue of $\hat{P}^{(H)}_{e,2}(T)$ over the ground state subspace.

The parity conservation reads $\hat{P}^{(H)}(T) = \hat{P}^{(H)}(0)$ leading to:

$$\hat{\gamma}_2(T)\,|\Psi_0\rangle = -\chi_1\chi_2\hat{\gamma}_1(0)\,|\Psi_0\rangle\,, \tag{14}$$

which corresponds to a MZM transport at the ground state level, and where $\chi_{1,2}$ can be explicitly computed for any specific example. If the process is adiabatic with respect to all possible energy differences in the spectrum, the same derivation holds for an arbitrary excited state $|\Psi_e\rangle$.

B. Majorana trijunction

We now apply the generic principles of adiabatic transport of MZMs outlined in the previous section to a trijunction[24,26,29–31], the simplest setup for braiding MZMs. The trijunction that we develop here braids MZMs by only tuning QD energy levels, and its elementary constituent is the QD-wire-QD setup displayed in Fig. 5 and described by the Hamiltonian:

$$\hat{H}_{\text{QD-K-QD}} = \hat{H}_{\text{QD-K}} + e'_d\hat{c}^\dagger\hat{c} - t_1\left(\hat{a}^\dagger_L\hat{c} + \hat{c}^\dagger\hat{a}_L\right). \tag{15}$$

Here, $\hat{H}_{\text{QD-K}}$ is in Eq. (1), e'_d is the energy level of the right QD, and $\hat{c}^{(\dagger)}$ is the fermionic annihilation (creation)

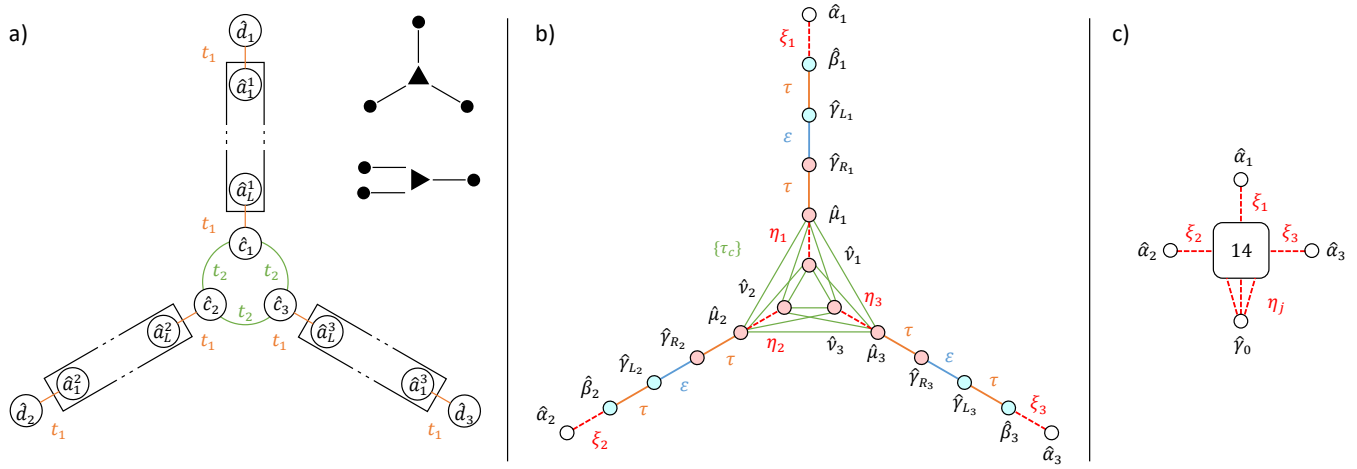

FIG. 4. a) The Majorana trijunction. It is built by connecting three identical QD-wire-QD systems through a hopping term t_2. A compact representation in given in the upper right corner, where a line stands for a Kitaev wire, a circle for a QD, and a triangle for 3 QDs connected by hopping terms; note that the trijunction we propose can in principle be realized with parallel nanowires. b) The low-energy behaviour of this system is captured by a set of 18 Majorana fermions (see Eq. (20)). c) The entire system amounts to 4 MZMs $\hat{\alpha}_1$, $\hat{\alpha}_2$, $\hat{\alpha}_3$ and $\hat{\gamma}_0$ connected to a network of 14 Majorana fermions by tunable couplings ξ_j, η_j.

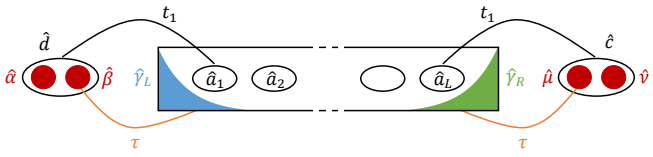

FIG. 5. Scheme of a QD-wire-QD setup: two QDs with a single fermionic mode are connected to the edges of a Kitaev wire through a real hopping amplitude t_1. The low-energy subspace is described by six Majorana modes $\hat{\alpha}$, $\hat{\beta}$ (left QD), $\hat{\mu}$, $\hat{\nu}$ (right QD) and $\hat{\gamma}_L$, $\hat{\gamma}_R$ (wire, exponentially localized at the edges). The effective couplings τ between the QD and the wire are defined in Eq. (16) and shown in the figure.

operator on this QD. For simplicity, both QDs are connected to the wire by the same hopping term t_1. The associated low-energy effective model in the *bowtie* configuration is:

$$\hat{H}^{\text{eff}}_{\text{QD-K-QD}} = i\left(\xi\hat{\alpha}\hat{\beta} + \eta\hat{\mu}\hat{\nu} + \varepsilon\hat{\gamma}_L\hat{\gamma}_R + \tau\,\hat{\beta}\hat{\gamma}_L + \tau\,\hat{\mu}\hat{\gamma}_R\right) \tag{16}$$

where $\hat{\mu}$ and $\hat{\nu}$ are the Majorana fermions of the right QD, and where $\eta = e'_d/2$. Note that we have changed the notation τ_L used in Eq. (2) into τ to avoid confusions. An important feature of Eq. (16) is that the coupling between the right dot and the Kitaev wire only involves the Majorana fermions $\hat{\mu}$ and $\hat{\gamma}_R$. In particular, setting $\eta = 0$ automatically localizes a MZM on $\hat{\nu}$.

We now examine the trijunction pictured in Fig. 4, panel a). It is built by tunnel-coupling the inner QDs of three QD-wire-QD devices, as described by the Hamiltonian:

$$\hat{H}_c = t_2\left(e^{i\phi_{12}}\hat{c}_1^\dagger\hat{c}_2 + e^{i\phi_{23}}\hat{c}_2^\dagger\hat{c}_3 + e^{i\phi_{31}}\hat{c}_3^\dagger\hat{c}_1 + \text{h.c.}\right); \tag{17}$$

the phases depend on the microscopic details of the contacts to the Kitaev wires, and they can be adjusted with a magnetic flux threading the inner QDs. For simplicity, the absolute values of the tunnel amplitudes are identical.

We begin our discussion by focusing on the inner part of the trijunction:

$$\hat{H}_{3\text{QD}} = i\sum_{j=1}^{3}\eta_j\hat{\mu}_j\hat{\nu}_j + \hat{H}_c. \tag{18}$$

where $\hat{c}_j = \frac{1}{2}(\hat{\mu}_j + i\hat{\nu}_j)$. For $\phi_{12} = \phi_{23} = \phi_{31} = \pi/6$ and $\eta_j = -\sqrt{3}t_2$, the model hosts a fermionic zero-mode $\frac{1}{\sqrt{3}}\sum_j \hat{c}_j$ corresponding to two MZMs; one of them is simply:

$$\hat{\gamma}_0 = \frac{1}{\sqrt{3}}\sum_{j=1}^{3}\hat{\nu}_j. \tag{19}$$

Importantly for the following discussion, it only contains the Majorana operators $\hat{\nu}_j$. For generic values of the phases ϕ_{ij} and for absolute values of the tunnel amplitudes that are not identical, one can still tune the energy of the inner QDs so that a MZM is localized only on operators $\hat{\nu}_j$, but the energies of the three QDs η_j will need to be tuned to different values, dubbed $\eta_{j,0}$. However, if $\phi_{12} + \phi_{23} + \phi_{31} = 0 \mod(\pi)$ an undesired degeneracy appears, and if any of the phases ϕ_{ij} vanishes, $\eta_{j,0} \to \infty$. These two latter situations should be carefully avoided in an experiment; the following discussion is generically valid for all other cases.

The low-energy description of the full trijunction involves 18 Majorana fermions; the Hamiltonian, sketched

in Fig. 4, panel b), reads

$$\hat{H}^{\text{eff}}_{\text{3-junct.}} = \sum_{j=1}^{3} \hat{H}^{\text{eff}\,(j)}_{\text{QD-K-QD}} + \hat{H}_c. \tag{20}$$

For simplicity, the couplings in the different wires are chosen to be identical except for the tunable QD energies ξ_j. Interestingly, at $\eta_j = \eta_{j,0}$, $\hat{\gamma}_0$ in Eq. (19) is not coupled to the Kitaev wires by the hopping τ and thus remains a MZM localized within the three inner QDs. We conclude that for $\xi_j = 0$ and $\eta_j = \eta_{j,0}$, the MZMs $\hat{\alpha}_1$, $\hat{\alpha}_2$, $\hat{\alpha}_3$ and $\hat{\gamma}_0$ decouple from the rest. The entire system can be thought of as four MZMs $\{\hat{\alpha}_j, \hat{\gamma}_0\}$ connected to a network of 14 Majorana fermions by tunable coupling amplitudes $\{\xi_j, \eta_j\}$, as sketched in Fig. 4, panel c).

Note that the derivation of this simple picture only requires that all energies involved in the effective Hamiltonian (20) are small with respect to the superconducting gap of the wires; that is $\varepsilon, \tau, t_2, \eta_j, \xi_j \ll |\Delta|$. These conditions are convenient for discussing the braiding procedure presented in Sec. III C, but they can be further released: if τ is increased, the MZMs start leaking into the wires and are no longer strictly localized on QDs; however, the system still features exact and (exponentially) localized MZMs. For large values of ξ_j, η_j, the QDs are anyway effectively decoupled from the modes $\hat{\alpha}_j, \hat{\gamma}_0$, regardless of their mixing with the bulk states of the wire. In the recent experiments performed by Deng *et al.*[50,51] on a QD coupled to a Kitaev wire, $|\Delta| \sim 200$ μeV, and $|\tau| \sim 100$ μeV (extracted from experimental data of Ref. 51). The *bowtie* pattern of Fig. 2 has been reproduced experimentally with $|\varepsilon|$ appearing to be of the order of the μeV.

C. Braiding protocol

As depicted in Fig. 4 (c), we identified for the trijunction four MZM under the fine-tuned condition $\xi_j = 0$, $\eta_j = \eta_{j,0}$. We now show that by moving away from this point, we can implement transport of Majorana fermions following the principles laid out in Sec. III A. We discuss in particular a protocol braiding $\hat{\alpha}_2$ and $\hat{\alpha}_3$ by manipulating the QD energies. We tune $\eta_j \neq \eta_{j,0}$ during the whole protocol: the system, illustrated in Fig. 6, is composed of 3 MZMs $\hat{\alpha}_j$ connected to a network of 15 Majorana fermions by three tunable couplings ξ_j. At the initial time $t = 0$, we set $\xi_2 = \xi_3 = 0$, and $\xi_1 = \xi_{\max} \neq 0$. The precise value of $\xi_{\max}$ is not important as long as it satisfies the condition $\xi_{\max} \ll \Delta$. The modes $\hat{\alpha}_2$ and $\hat{\alpha}_3$ host clearly localized MZMs and the ground state is doubly degenerate.

The braiding protocol follows the one proposed in Ref. 30 and consists in moving across the system one MZM at each step, following the scheme explained in Fig. 3, right panel. It requires 7 steps, which are summarized in Table I and illustrated in Fig. 6: $\hat{\alpha}_2$ is moved to position 1 (where $\hat{\alpha}_1$ was), then $\hat{\alpha}_3$ to position 2 and finally $\hat{\alpha}_2$ to position 3. The overall effect is to interchange

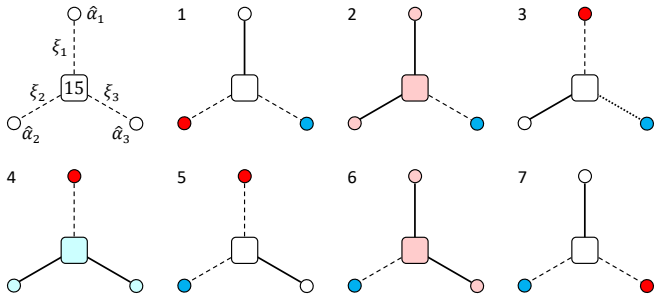

FIG. 6. Braiding procedure exchanging the positions of the MZMs $\hat{\alpha}_2$ (red) and $\hat{\alpha}_3$ (blue). Couplings ξ_j are switched between $\xi_{\max}$ (coupling *on*, solid line) and 0 (coupling *off*, dashed line) by tuning the QD energies. The entire protocol is based on three replicas of the transport scheme of Fig. 3, right panel. During the entire procedure, the ground state is twofold degenerate. The QD energies ξ_j in steps $1 \ldots 7$ are summarized in Table I.

Step	ξ'_1	ξ'_2	ξ'_3	$\hat{\alpha}_1(t)$	$\hat{\alpha}_2(t)$	$\hat{\alpha}_3(t)$
1	$\xi_{\max}$	0	0	$*$	$\hat{\alpha}_2$	$\hat{\alpha}_3$
2	$\xi_{\max}$	$\xi_{\max}$	0	$*$	$*$	$\hat{\alpha}_3$
3	0	$\xi_{\max}$	0	$-\hat{\alpha}_2$	$*$	$\hat{\alpha}_3$
4	0	$\xi_{\max}$	$\xi_{\max}$	$-\hat{\alpha}_2$	$*$	$*$
5	0	0	$\xi_{\max}$	$-\hat{\alpha}_2$	$-\hat{\alpha}_3$	$*$
6	$\xi_{\max}$	0	$\xi_{\max}$	$*$	$-\hat{\alpha}_3$	$*$
7	$\xi_{\max}$	0	0	$*$	$-\hat{\alpha}_3$	$\hat{\alpha}_2$

TABLE I. QD energies ξ_j at each step of the braiding protocol described in Fig. 6, and tracking of the initial MZMs $\hat{\alpha}_i$ through the transport steps. A star $(*)$ indicates that $\hat{\alpha}_i(t)$ does not correspond to a MZM. The C_3 symmetry of the trijunction imposes $\chi_1 = \chi_2$ in Eq. (14), and provides a simple way of keeping track of the signs.

$\hat{\alpha}_2$ and $\hat{\alpha}_3$. $\hat{\alpha}_1$ plays no direct role in the exchange except for the fact that its position is used as a storage buffer for $\hat{\alpha}_2$. During the entire procedure, the ground state is twofold degenerate, and higher energy levels are gapped by an energy $E'_G \geq \mathcal{O}\left(\min(\tau, t_2, \varepsilon, \xi_{\max})\right)$ which fixes a timescale for adiabaticity. Experimentally, ε appears to be the smallest parameter[50,51]; for $\varepsilon \sim 1$ μeV transport experiments shall be performed at frequency well below the GHz regime.

The full braiding operation after time T transfers the MZMs as

$$\hat{\alpha}_2(T) = -\zeta\hat{\alpha}_3 \qquad \hat{\alpha}_3(T) = \zeta\hat{\alpha}_2, \tag{21}$$

where we have written $\hat{\alpha}_j$ for $\hat{\alpha}_j(0)$, and where $\zeta = \pm 1$ is the chirality of the braiding[25]; in Fig. 6 and Table I, $\zeta = 1$. The associated unitary time-evolution operator is[12]:

$$\hat{U}_{23} = \exp\left(\frac{\pi}{4}\zeta\hat{\alpha}_2\hat{\alpha}_3\right) = \frac{1}{\sqrt{2}}\left(1 + \zeta\hat{\alpha}_2\hat{\alpha}_3\right), \tag{22}$$

so that $\hat{\alpha}_j(T) = \hat{U}^\dagger_{23}\hat{\alpha}_j\hat{U}_{23}$.

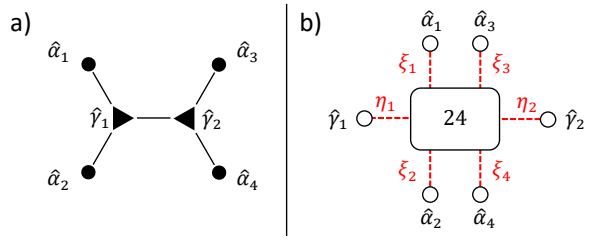

FIG. 7. a) Circuit with 5 Kitaev wires (solid lines), and two trijunctions (triangles) hosting six MZMs. The outer QDs (circles) allow for parity measurements. b) The circuit breaks down to 6 MZMs $\{\hat{\alpha}_{1\ldots4}, \hat{\gamma}_{1,2}\}$ connected to a network of 24 Majorana fermions by tunable couplings ξ_j, η_j.

Repeating the braiding twice results in a non-trivial operation on the degenerate ground state:

$$\left(\hat{U}_{23}\right)^2 = \zeta \hat{\alpha}_2 \hat{\alpha}_3. \tag{23}$$

This is the signature of the non-Abelian statistics of the MZMs. One recovers the initial state (up to a global phase) only after performing the braiding 4 times.

D. Experimental demonstration of non-Abelian statistics

The previous setup allows to braid two MZMs, but the time-evolution operator $\hat{U}_{23}$ in Eq. (22) commutes with the parity $\hat{P}_{23} = i\hat{\alpha}_2\hat{\alpha}_3$. This limits the operations that can be performed on the twofold degenerate ground space through braiding to a dephasing between the even-parity and odd-parity states, which cannot be measured experimentally. This issue can be circumvented by increasing the number of MZMs so that for fixed parity the ground space is degenerate[7]; in the following, we propose and discuss a setup hosting six MZMs.

We assemble 5 Kitaev wires so that they form two trijunctions as shown in Fig. 7, panel a). With arguments similar to those presented in Sec. III B, we obtain that the subgap physics is composed of 6 MZMs $\{\hat{\alpha}_1, \hat{\alpha}_2, \hat{\alpha}_3, \hat{\alpha}_4, \hat{\gamma}_1, \hat{\gamma}_2\}$ connected to a network of 24 Majorana fermions by tunable couplings ξ_j, η_j[73] (see Fig. 7, panel b). At the beginning two couplings are set out of resonance, for instance $\xi_3 = \xi_4 = \xi_{\max}$. The four remaining MZMs are strictly localized on $\{\hat{\alpha}_1, \hat{\alpha}_2, \hat{\gamma}_1, \hat{\gamma}_2\}$, and the ground space is fourfold degenerate. If we define the total parity $\hat{P}_{1122} = -\hat{\alpha}_1\hat{\alpha}_2\hat{\gamma}_1\hat{\gamma}_2$, two ground states have even parity and two have odd parity.

In Fig. 8, panel a), we show how to braid $\hat{\gamma}_1$ and $\hat{\gamma}_2$ by only tuning QD energies; even if the time-evolution operator $\exp\left[\frac{\pi}{4}\zeta\hat{\gamma}_1\hat{\gamma}_2\right]$ commutes with $\hat{P}_{1122}$, the non-Abelian statistics can be experimentally demonstrated. The idea is to measure the parity $\hat{P}_{11} = i\hat{\alpha}_1\hat{\gamma}_1$ before and after performing two consecutive braidings of $\hat{\gamma}_1$ and $\hat{\gamma}_2$. These two consecutive braidings amount to the operation $\hat{\gamma}_{1,2} \to -\hat{\gamma}_{1,2}$ as in Eq. (23), and therefore imply

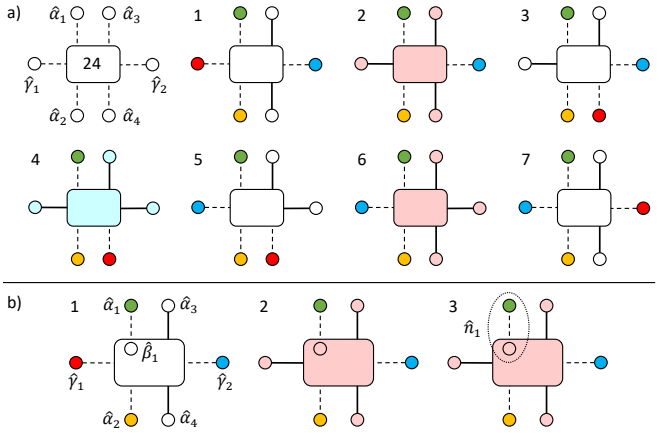

FIG. 8. a) Braiding of $\hat{\gamma}_1$ (red) and $\hat{\gamma}_2$ (blue). The couplings are modified in time, similarly to the protocol presented in Sec. III C; dashed lines indicate that a coupling is *off* (QD energy at resonance), and solid lines stand for couplings *on* (QD energy out of resonance). b) Charge measurement used to infer the parity $\hat{P}_{11} = i\hat{\alpha}_1\hat{\gamma}_1$. η_1 is set out of resonance, so that the MZM initially localized on $\hat{\gamma}_1$ (red) expands over the entire network. In particular, it acquires a nonzero component on $\hat{\beta}_1$, which is the second Majorana mode of the QD hosting $\hat{\alpha}_1$ (green). The charge measured on this QD is correlated to the parity $\hat{P}_{11}$, as described in Eq. (25).

$\hat{P}_{11} \to -\hat{P}_{11}$. Because the initial and the final Hamiltonians are identical, this parity switch is a signature of the non-Abelian nature of MZMs[74].

We now outline a simple protocol that gives some information about the parity $\hat{P}_{11}$; it is sketched in Fig 8, panel b): starting from the initial situation with $\xi_3 = \xi_4 = \xi_{\max}$, we adiabatically tune the energy η_j of the three quantum dots in the first trijunction to the out-of-resonance value $\eta_{\max}$. As a consequence, the MZM initially localized on $\hat{\gamma}_1$ spreads over the entire network. We call $\hat{\gamma}_1'$ this delocalized MZM and, because of adiabaticity, $\hat{P}_{11} = \hat{P}_{11}'$ where $\hat{P}_{11}' = i\hat{\alpha}_1\hat{\gamma}_1'$. In particular, $\hat{\gamma}_1'$ acquires a nonzero component u on $\hat{\beta}_1$, but no component on the decoupled MZM $\hat{\alpha}_1$. As such, the measurement of the occupation of the QD 1:

$$\hat{n}_1 = \frac{1}{2}\left(1 + i\hat{\alpha}_1\hat{\beta}_1\right), \tag{24}$$

can distinguish between two parity states of $\hat{P}_{11}$ with an accuracy fixed by u. More precisely, if the system is in an eigenstate of $\hat{P}_{11}$ with parity p, the expectation value of $\hat{n}_1$ is (see Appendix B 1):

$$\langle \hat{n}_1 \rangle_p = \frac{1}{2}(1 + up). \tag{25}$$

Many experimental techniques allow for this charge measurement; for instance, it can be performed with a quantum point contact placed nearby, or through microwave reflection[75–86]. Because $|u| < 1$, this measurement does not correspond to an exact readout of the parity $\hat{P}_{11}$, and the final state is projected into a tilted basis

(the charge eigenstates instead of the parity eigenstates). Therefore, the non-Abelian nature of the MZMs should be deduced by accumulating statistics on the outcome of the two charge measurements (before and after braiding). In a circuit with uniform tunnel couplings τ, u saturates at $1/\sqrt{5}$, but it can be further increased by releasing this constraint (see Appendix B 2). Alternatively, one can use the more sophisticated measurement scheme presented in Appendix B 3, which allows for an exact measurement of $\hat{P}_{11}$. Note that these measurement schemes can also read out parities of type $i\hat{\alpha}_j\hat{\alpha}_k$, and that they recycle the QDs originally used for braiding into parity meters.

IV. TOPOLOGICAL QUANTUM COMPUTATION IN QD-CONTROLLED CIRCUITS

The setup presented in Sec. III D and sketched in Fig. 7 provides two zero-energy states for a fixed parity, which can be used as a logical qubit. It is encoded by four MZMs, renamed $\hat{\gamma}_{1\ldots4}$ for simplicity, that are spatially separated in the circuit: quantum information is stored non-locally and therefore enjoys topological protection. A representation of the logical Pauli matrices on both parity sectors is given by:

$$\bar{\sigma}_x = -i\hat{\gamma}_1\hat{\gamma}_2 \qquad \bar{\sigma}_y = -i\hat{\gamma}_2\hat{\gamma}_3 \qquad \bar{\sigma}_z = -i\hat{\gamma}_1\hat{\gamma}_3, \quad (26)$$

and we define the logical states $|\bar{0}\rangle$ and $|\bar{1}\rangle$ as the eigenvectors of $\bar{\sigma}_z$.

Manipulations of the MZMs perform quantum logical operations, and the braiding of MZMs $\hat{\gamma}_i$ and $\hat{\gamma}_j$ with chirality $\zeta = \pm1$ according to the protocol shown in Fig 8, panel a) is described by the time-evolution operator:

$$\hat{U}_{ij} = \exp\left(\frac{\pi}{4}\zeta\hat{\gamma}_i\hat{\gamma}_j\right). \quad (27)$$

Braiding operations therefore implement discrete single-qubit $\pi/2$ rotations along the x, y and z axis of the Bloch sphere defined by Eq. (26). A standard choice for reaching universality is to complete them with the single-qubit $\pi/8$ phase gate T and the two-qubits controlled σ_z gate $\Lambda(\sigma_z)$.

An implementation of $\Lambda(\sigma_z)$ with QD-controlled circuits is given in Sec. IV A; it is achieved using braiding operations together with projective measurements of 4-MZMs parities. The implementation of the T gate is discussed in Sec. IV B, and relies on magic state distillation instead of topological protection.

A. 4-MZMs parity measurement and $\Lambda(\sigma_z)$ gate

Let us consider two replicas a and b of our single-qubit circuit. Both of them operate four MZMs, $\hat{\gamma}^a_{1\ldots4}$ and $\hat{\gamma}^b_{1\ldots4}$ respectively, which encode the topological qubits $|q_a\rangle$ and $|q_b\rangle$. Despite MZMs from different circuits cannot be braided, it has been shown that a controlled σ_z gate over $|q_a\rangle \otimes |q_b\rangle$ could be implemented only through braiding and projective parity measurements[37,39]. Braiding and parity readout are the natural operations one can perform with MZMs, and together with the $\Lambda(\sigma_z)$, they implement the set of gates known as the Clifford group. The exact scheme for a $\Lambda(\sigma_z)$ gate based only on these natural operations is shown in Appendix C; here we only discuss its feasibility in QD-controlled circuits. In addition to on-circuit braiding and on-circuit parity readout (implemented in Sec. III D), the procedure requires:

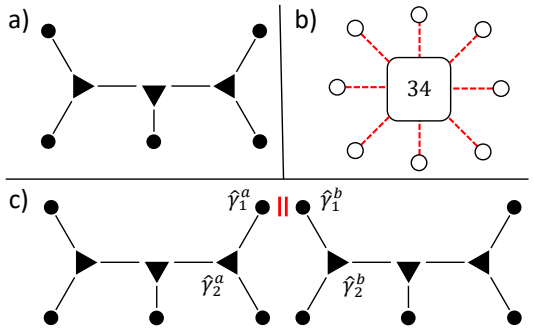

FIG. 9. a) 2-qubits circuit allowing for the implementation of a $\Lambda(\sigma_z)$ gate. b) It amounts to 8 Majorana fermions coupled to a network; 2 are gapped and serve for transport purposes, and the 6 remaining ones store two qubits: a logical qubit and an ancilla. c) 4-MZMs parity measurement between two 2-qubits circuits. The simple parities $\hat{P}^a_{12} = i\hat{\gamma}^a_1\hat{\gamma}^a_2$ and $\hat{P}^b_{12} = i\hat{\gamma}^b_1\hat{\gamma}^b_2$ can be perfectly correlated with the charges q_a and q_b on the neighbouring QDs. A parity meter (red bars ||) measuring the parity of the total charge $Q = q_a + q_b$ performs a projective measurement of the 4-MZMs parity $\hat{P}_{1212} = -\hat{\gamma}^a_1\hat{\gamma}^a_2\hat{\gamma}^b_1\hat{\gamma}^b_2$.

(i) An ancillary pair of MZMs lying on the physical circuit of the target qubit.

(ii) Projective measurement of a 4-MZMs parity of type:

$$\hat{P}_{jklm} = -\hat{\gamma}^a_j\hat{\gamma}^a_k\hat{\gamma}^b_l\hat{\gamma}^b_m. \quad (28)$$

The ancillary pair of MZMs can be provided by increasing the size of our elementary circuit: a version involving three trijunctions and 8 tunable Majorana fermions, therefore providing 6 computational MZMs and hosting two qubits (later called *2-qubits circuit*), is sketched in Fig. 9, panels b) and c). For simplicity, we will not distinguish between the control and the target qubit, and we will store both of them on such a scaled-up circuit. The computational MZMs are from now on $\hat{\gamma}^a_{1\ldots6}$ and $\hat{\gamma}^b_{1\ldots6}$. Braiding and parity readout schemes inside these circuits is analogous to those of Fig. 8.

In Sec. III D and Appendix B, we have shown how the parities $\hat{P}^a_{jk} = i\hat{\gamma}^a_j\hat{\gamma}^a_k$ and $\hat{P}^b_{lm} = i\hat{\gamma}^b_l\hat{\gamma}^b_m$ could be perfectly correlated with the occupation number of QD a_j (hosting $\hat{\gamma}^a_j$) and QD b_l (hosting $\hat{\gamma}^b_l$) respectively. Therefore, measuring the total charge parity of the system made of QDs a_j and b_l amounts to a projective measurement of

$\hat{P}^a_{jk}\hat{P}^b_{lm} = \hat{P}_{jklm}$. This can be considered experimentally if these two QDs are placed nearby (see Fig. 9, panel a): there have been proposals for building charge parity meters, either with a quantum point contact placed between the two adjacent QDs[87], or through microwave reflection[88].

B. Magic state distillation and $\pi/8$ phase gate

A direct consequence of the Gottesman-Knill theorem[89] is that operations of the Clifford group are not sufficient to implement the T quantum gate. One could of course use unprotected operations in order to implement it, but the resulting errors would spoil the benefits of topological quantum computation. For example, splitting the two logical states of a qubit in energy during a precise period could amount to a $\pi/4$ relative phase, and this could be done in a QD-controlled circuit by coupling two computational MZMs.

An efficient implementation of the T gate can still be achieved. It relies on error correcting codes, and is known *magic state distillation*[38,39]. Let us assume that we want to operate the T gate on a logical qubit $|q_1\rangle$, and that we have access to a second qubit prepared in the *magic state*:

$$|H\rangle = \frac{1}{\sqrt{2}}\left(|0\rangle + e^{i\pi/4}|1\rangle\right). \tag{29}$$

Then, applying a proper set of Clifford gates on $|H\rangle\otimes|q_1\rangle$ (implemented in Sec. IV A) amounts to performing a T gate on $|q_1\rangle$[7].

Of course, a magic state cannot be prepared with the Clifford group, but it can be approached with good accuracy by *distillation protocols*[38,39,90–94]. Such schemes require several noisy copies $\{|H'_i\rangle\}$ of $|H\rangle$, that can be obtained through unprotected operations. A distillation step consists in measuring a set of stabilizers on $\{|H'_i\rangle\}$, and in implementing some corresponding corrections; if the initial error on $\{|H'_i\rangle\}$ are small enough, the protocol builds a converging copy of $|H\rangle$. Importantly, the distillation routine only relies on the Clifford group, and can therefore be implemented in QD-controlled circuits. In a topological quantum processor, distillation protocols should run continuously in dedicated registers, so that magic states are always available when needed for a logical operation.

C. Scaling up

A straight-forward way of scaling up a QD-controlled topological quantum processor is to build a network of 2-qubits circuits, each of them hosting a single logical qubit and one ancilla (needed for the controlled σ_z operation). As such, two-qubit operations can be performed on neighbouring sites through 4-MZMs parity measurements, and quantum information is encoded in a sparse way, which prevents local errors from propagating. An example of such architecture, which can virtually be extended at will, is given in Fig. 10.

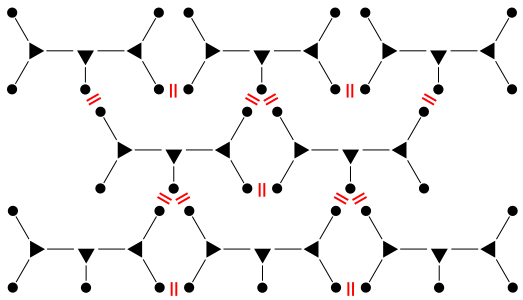

FIG. 10. Network of 8 replicas of the 2-qubits circuit (one logical qubit and one ancilla) presented in Sec. IV A, virtually connected by QD charge parity meters (red bars ||). This device amounts to a 8-qubit topological quantum processor, and the underlying pattern can be scaled-up at will.

V. CONCLUSIONS

Motivated by the recent experimental realization of a nanowire hosting MZMs coupled to a single QD[50,51], we discussed a network of Kitaev's wires coupled to tunable QDs where topologically-protected operations can be achieved by solely manipulating the QDs. In particular, we described in details a trijunction with six QDs where the non-Abelian statistics of the MZMs can be revealed, and outlined ideas for scaling up the network to more advanced purposes. These results show the exceptional versatility and usefulness of hybrid nanowire-QD devices that are currently produced in laboratories.

ACKNOWLEDGMENTS

We thank M. Burrello and A. Stern for enlightening observations and comments; we also gratefully acknowledge discussions with N. Clausen, V. Crepel and J. Lebreuilly. L. Mazza was supported by LabEX ENS-ICFP: ANR-10-LABX-0010/ANR-10-IDEX-0001-02 PSL*. C. Mora acknowledges support from Idex PSL Research University (ANR-10- IDEX-0001-02 PSL)

Appendix A: Parity switch

The effective model for the QD-wire setup is in Eq. (2), which we reproduce here below for better readability:

$$\hat{H}^{\text{eff}}_{\text{QD-K}} = i\left(\xi\,\hat{\alpha}\hat{\beta} + \varepsilon\,\hat{\gamma}_L\hat{\gamma}_R + \tau_L\,\hat{\beta}\hat{\gamma}_L + \tau_R\hat{\alpha}\hat{\gamma}_R\right). \tag{A1}$$

It is a quadratic form of the vector $\{\hat{\alpha},\ \hat{\beta},\ \hat{\gamma}_L,\ \hat{\gamma}_R\}$:

$$\hat{H}^{\text{eff}}_{\text{QD-K}} = \frac{i}{2}\sum_{i,j} x_i A_{ij} x_j, \qquad \vec{x}^T = \begin{pmatrix} \hat{\alpha} & \hat{\beta} & \hat{\gamma}_L & \hat{\gamma}_R \end{pmatrix}; \tag{A2}$$

where:

$$A_{i,j} = \begin{pmatrix} 0 & \xi & 0 & \tau_R \\ -\xi & 0 & \tau_L & 0 \\ 0 & -\tau_L & 0 & \varepsilon \\ -\tau_R & 0 & -\varepsilon & 0 \end{pmatrix}. \tag{A3}$$

The condition for $\hat{H}^{\text{eff}}_{\text{QD-K}}$ to exhibit MZMs is:

$$0 = \text{Det } A_{ij} = \left(\varepsilon\xi + \tau_L\tau_R\right)^2; \tag{A4}$$

and we recover the position of the parity switch given in Eq. (3).

Appendix B: Parity readout

1. Simple readout protocol

The readout protocol proposed in Sec. III D aims at measuring the parity $\hat{P}_{11}(0) = i\hat{\alpha}_1(0)\hat{\gamma}_1(0)$. During a first step, the couplings η_j of the first trijunction are tuned out of resonance while the MZMs $\{\hat{\alpha}_1, \hat{\alpha}_2, \hat{\gamma}_2\}$ are kept uncoupled, so that after a time T_1:

$$\begin{aligned} &\hat{\alpha}_1(0) = \hat{\alpha}_1(T) \qquad \hat{\alpha}_2(0) = \hat{\alpha}_2(T) \qquad \hat{\gamma}_2(0) = \hat{\gamma}_2(T) \\ &\hat{\gamma}_1(0) = u\hat{\beta}_1(T) + \sum_j v_j \hat{\delta}_j(T), \end{aligned} \tag{B1}$$

where the set $\{\hat{\delta}_j(T)\}$ stands for all Majorana fermions of the effective model, except for $\{\hat{\alpha}_1(T), \hat{\alpha}_2(T), \hat{\gamma}_2(T)\}$ and $\hat{\beta}_1(T)$. Therefore:

$$\begin{aligned} \hat{P}_{11}(0) &= i\hat{\alpha}_1(0)\hat{\gamma}_1(0) \\ &= iu\hat{\alpha}_1(T)\hat{\beta}_1(T) + \sum_j iv_j\hat{\alpha}_1(T)\hat{\delta}_j(T) \end{aligned} \tag{B2}$$

We now measure the occupation of QD 1. Its expectation value on a state $|\psi\rangle$ is:

$$\langle\psi|\,\hat{n}_1(T)\,|\psi\rangle = \frac{1}{2}\left(1 + \langle\psi|\,i\hat{\alpha}_1(T)\hat{\beta}_1(T)\,|\psi\rangle\right). \tag{B3}$$

If the system is in an eigenstate $|\psi_p\rangle$ of $\hat{P}_{11}(0)$ with parity $p = \pm 1$, we can enforce the equality:

$$\begin{aligned} &\langle\psi_p|\,i\hat{\alpha}_1(T)\hat{\beta}_1(T)\,|\psi_p\rangle = \\ &\qquad = \frac{p}{2}\langle\psi_p|\,\{i\hat{\alpha}_1(T)\hat{\beta}_1(T), \hat{P}_{11}(0)\}\,|\psi_p\rangle\,. \end{aligned} \tag{B4}$$

In the decomposition (B2), all terms of $\hat{P}_{11}(0)$, except for the first one, anticommute with $i\hat{\alpha}_1(T)\hat{\beta}_1(T)$. Therefore:

$$\begin{aligned} &\langle\psi_p|i\hat{\alpha}_1(T)\hat{\beta}_1(T)\,|\psi_p\rangle = \\ &\quad = \frac{p}{2}\langle\psi_p|\,\{i\hat{\alpha}_1(T)\hat{\beta}_1(T), iu\hat{\alpha}_1(T)\hat{\beta}_1(T)\}\,|\psi_p\rangle \\ &\quad = up, \end{aligned} \tag{B5}$$

and as stated in Sec. III D:

$$\langle\psi_p|\,\hat{n}_1(T)\,|\psi_p\rangle = \frac{1}{2}\left(1 + up\right) \tag{B6}$$

Note that the MZMs $\hat{\alpha}_2$ and $\hat{\gamma}_2$, which remain uncoupled during the entire procedure and upon which no measurement is performed, are not affected by this measurement.

2. Accuracy

The accuracy of the previous protocol is set by the weight u of the delocalized MZM in Eq. (B1), where $|u| = 1$ corresponds to a perfect measurement and $|u| = 0$ gives no information about the parity (see Eq. (B6)). We have previously set $\xi_3 = \xi_4 = \xi_{\max}$ and $\eta_1 = \eta_{\max}$ (situation 2 of Fig. 8, panel b); in the limit $\xi_{\max}, \eta_{\max} \to \infty$, we find the simple expression:

$$|u| = \frac{|r|}{\sqrt{5r^2+5}}, \qquad r = \frac{\varepsilon}{\tau}, \tag{B7}$$

which is maximal for a weakly coupled QD ($r^2 \ll 1$) and saturates at $1/\sqrt{5} \approx 0.45$.

This factor actually arises from the delocalized MZM spreading uniformly among the resonant QDs (one hosting $\hat{\alpha}_1$, one hosting $\hat{\alpha}_2$ and three hosting $\hat{\gamma}_2$). In principle, this spreading could be biased by taking non-uniform physical parameters for the circuit. More precisely, if $\tau_{1,2}$ are the tunnel couplings of the outer QDs hosting $\hat{\alpha}_{1,2}$, $\varepsilon_{1,2}$ the energy splittings of their adjacent Kitaev wires, τ_0 the tunnel coupling of the inner QDs to the wires and ε_0 the energy splitting of the central wire, then in the same limit $\xi_{\max}, \eta_{\max} \to \infty$:

$$|u| = \frac{|r_1|}{\sqrt{r_1^2 + r_2^2 + 3r_0^2 + 5}}, \qquad r_j = \frac{\varepsilon_j}{\tau_j}, \tag{B8}$$

and $|u| = 1$ in the limit where only the QD 1 is weakly coupled.

3. Exact parity measurement

An intuitive idea for reading out the parity of a topological system consists in splitting the even, and odd states in energy and then performing some spectroscopic measurement. If one can turn the existing QDs of the system into a spectrometer, exact parity readout is achieved without any additional cost. Such a protocol was put forward in Ref. 71, where Rabi oscillations between a QD and a Kitaev wire are used to determine the parity of the degenerate ground state.

Let us start with situation 2 of Fig. 8 (b), where the MZMs of the system are described by Eq. (B1). Adiabatically tuning ξ_1 out of resonance introduces a coupling between $\hat{\alpha}_1(T)$ and $\hat{\beta}_1(T)$, and therefore splits the two

parity states in energy. Tuning it further away up to the limit $\xi_1 = -\infty$, still adiabatically, charges the QD 1 and effectively uncouples it from the rest of the system: eigenstates of the total effective model are eigenstates of $\hat{n}_1$. At this point, the two parity eigenstates have been split by an energy $2\varepsilon_0$, which we assume to be much smaller than the other non-zero energy states of the Hamiltonian. The energy of QD 1 is quickly set at $\xi_1 = -\varepsilon_0$, allowing for Rabi oscillations between the QD and the rest of the system thanks to the coupling term:

$$\hat{H}_\tau = i\tau\hat{\beta}_1\hat{\gamma}_{L_1}. \tag{B9}$$

Importantly:

(i) The Hamiltonian is still twofold degenerate because of the MZMs $\hat{\alpha}_2$ and $\hat{\gamma}_2$, but as they are strictly localized onto their respective QDs, they do not get coupled by $\hat{H}_\tau$.

(ii) The Majorana modes defining the parity eigenstate have a non-zero component u on $\hat{\gamma}_{L_1}$, so that they get coupled to the QD 1.

(iii) We assume that all other energy levels are separated from $\pm\varepsilon_0$ by an energy much larger than τ, so that spurious subgap states are effectively uncoupled from the dot.

With these conditions, the dynamics is reduced to Rabi oscillations occurring between the QD 1 and the parity eigenstate. In the Fock basis associated to this subspace, the Hamiltonian reads[64,71]:

$$\begin{aligned}\hat{H}_{\text{Rabi}} = &\begin{pmatrix} |00\rangle \\ |11\rangle \end{pmatrix}^T \begin{pmatrix} 0 & u\tau/2 \\ u\tau/2 & \varepsilon_0+\xi_1 \end{pmatrix} \begin{pmatrix} \langle 00| \\ \langle 11| \end{pmatrix} \\ &+ \begin{pmatrix} |01\rangle \\ |10\rangle \end{pmatrix}^T \begin{pmatrix} \varepsilon_0 & u\tau/2 \\ u\tau/2 & \xi_1 \end{pmatrix} \begin{pmatrix} \langle 01| \\ \langle 10| \end{pmatrix}.\end{aligned} \tag{B10}$$

Having tuned $\xi_1 = -\varepsilon_0$ sets the Rabi process $|00\rangle \leftrightarrow |11\rangle$ on resonance, while $|01\rangle \leftrightarrow |10\rangle$ is out of resonance. We assume that the QD is weakly coupled to the wire, that is $(u\tau)^2 \ll \varepsilon_0^2$, so that this second process is completely suppressed.

Because the QD was initially charged, the system starts either in state $|10\rangle$, and its dynamics is frozen, or in state $|11\rangle$, and it undergoes full Rabi oscillations with $|00\rangle$ at a frequency $\omega_0 = u\tau/2$. Therefore, after half a Rabi oscillation, a charge measurement on the QD can perfectly distinguish between the initial parity states. At this precise moment, the QD energy is quickly tuned out of resonance: the QD charge has been perfectly correlated with the parity we need to measure, and can now be read out by charge sensing, or be used in a 4-MZMs parity measurement (see Sec. IV A).

The significant advantage of this method is that the accuracy no longer saturates at $1/\sqrt{5}$ in the limit of a weakly coupled QD, essentially because QD 1 plays a privileged role. Also, the constraint of a weakly coupled QD can in principle be further released. If the Rabi process $|01\rangle \leftrightarrow |10\rangle$ cannot be suppressed, it will occur with an detuned frequency $\omega_1 = \sqrt{\varepsilon_0^2 + (u\tau)^2}$; if the two Rabi processes are in perfect phase opposition at a time T_1, both parities can perfectly be distinguished. This can be ensured by adjusting $\eta_{\max}$ so that ω_1/ω_0 becomes a rational ratio.

Note however that this parity readout operation is not protected: an error in the duration of the Rabi oscillations will unavoidably result into an tilted projection basis.

Appendix C: Clifford-based $\Lambda(\sigma_z)$ gate

Here we reproduce an algorithm introduced in Refs 37 and 39. We want to implement a $\Lambda(\sigma_z)$ gate on two topological qubits $|q_a\rangle$ and $|q_b\rangle$ built on $\hat{\gamma}^a_{1\ldots4}$ and $\hat{\gamma}^b_{1\ldots4}$ respectively. If $|q_a\rangle$ is the control qubit and $|q_b\rangle$ the target, the controlled σ_z gate is:

$$\Lambda(\sigma_z) = \exp\left(i\frac{\pi}{4}(I-\bar{\sigma}^a_z)(I-\bar{\sigma}^b_z)\right) \tag{C1}$$

In terms of MZMs (see Eq. (26)):

$$\begin{aligned}\Lambda(\sigma_z) =& e^{i\pi/4}\exp\left(-\frac{\pi}{4}\hat{\gamma}^a_1\hat{\gamma}^a_3\right)\exp\left(-\frac{\pi}{4}\hat{\gamma}^b_1\hat{\gamma}^b_3\right) \\ &\times\exp\left(-i\frac{\pi}{4}\hat{\gamma}^a_1\hat{\gamma}^a_3\hat{\gamma}^b_1\hat{\gamma}^b_3\right)\end{aligned} \tag{C2}$$

The first two operations represent on-circuit braidings (see Eq. (27)), which have already been discussed. We focus on the implementation of the four MZM gate:

$$U^{(4)} = \exp\left(-i\frac{\pi}{4}\hat{\gamma}^a_1\hat{\gamma}^a_3\hat{\gamma}^b_1\hat{\gamma}^b_3\right) \tag{C3}$$

We assume that an ancillary pair of MZMs $\hat{\gamma}^b_5$ and $\hat{\gamma}^b_6$ lies on circuit b, and that it has been initialized in state $|0\rangle$ so that:

$$(\hat{\gamma}^b_5 + i\hat{\gamma}^b_6)\,|\psi\rangle = 0, \tag{C4}$$

where $|\psi\rangle$ is the initial wave function of the entire computational subspace.

We first measure the 4-MZMs parity $\hat{P}_{1335} = -\hat{\gamma}^a_1\hat{\gamma}^a_3\hat{\gamma}^b_3\hat{\gamma}^b_5$ (demonstrated in Sec. IV A), and depending on the output $p_1 = \pm1$, the initial wave function gets projected by:

$$\Pi_1^{(p_1)} = \frac{1}{2}\left(1 - p_1\hat{\gamma}^a_1\hat{\gamma}^a_3\hat{\gamma}^b_3\hat{\gamma}^b_5\right). \tag{C5}$$

We then measure the on-circuit parity $\hat{P}^b_{15} = i\hat{\gamma}^b_1\hat{\gamma}^b_5$. An outcome $p_2 = \pm1$ amounts to the projector:

$$\Pi_2^{(p_2)} = \frac{1}{2}\left(1 + p_2\hat{\gamma}^b_1\hat{\gamma}^b_5\right). \tag{C6}$$

Then, depending on the measured parities p_1 and p_2, corrective on-circuit braidings are performed so that the

final outcome amounts to applying $U^{(4)}$. More precisely, if the four possibilities for the projective measurements are $\Pi_{21}^{(p_2 p_1)} = \Pi_2^{(p_2)}\Pi_1^{(p_1)}$, with corresponding outcomes $(p_2, p_1) \in \{++, +-, -+, --\}$, these corrections are given by the four possible expansions:

$$\begin{aligned}
&\exp\left(-i\frac{\pi}{4}\hat{\gamma}_1^a\hat{\gamma}_3^a\hat{\gamma}_1^b\hat{\gamma}_3^b\right)|\psi\rangle = \\
&= 2\exp\left(-\frac{\pi}{4}\hat{\gamma}_1^b\hat{\gamma}_6^b\right)\Pi_{21}^{++}|\psi\rangle \\
&= 2i\exp\left(\frac{\pi}{2}\hat{\gamma}_1^a\hat{\gamma}_3^a\right)\exp\left(\frac{\pi}{2}\hat{\gamma}_1^b\hat{\gamma}_3^b\right)\exp\left(-\frac{\pi}{4}\hat{\gamma}_3^b\hat{\gamma}_6^b\right)\Pi_{21}^{+-}|\psi\rangle \\
&= 2i\exp\left(\frac{\pi}{2}\hat{\gamma}_1^a\hat{\gamma}_3^a\right)\exp\left(\frac{\pi}{2}\hat{\gamma}_1^b\hat{\gamma}_3^b\right)\exp\left(+\frac{\pi}{4}\hat{\gamma}_3^b\hat{\gamma}_6^b\right)\Pi_{21}^{-+}|\psi\rangle \\
&= 2\exp\left(+\frac{\pi}{4}\hat{\gamma}_1^b\hat{\gamma}_6^b\right)\Pi_{21}^{--}|\psi\rangle
\end{aligned} \tag{C7}$$

where the condition (C4) has been used.

In the end, the ancillary pair of MZMs $\hat{\gamma}_{5,6}^b$ is unchanged; however, it was essential for the practical implementation of the gate.

[1] E. Majorana, "Teoria simmetrica dell'elettrone e del positrone," Il Nuovo Cimento (1924-1942) **14**, 171 (2008).
[2] J. Alicea, "New directions in the pursuit of majorana fermions in solid state systems," Rep. Prog. Phys. **75**, 076501 (2012).
[3] M. Leijnse and K. Flensberg, "Introduction to topological superconductivity and majorana fermions," Semiconductor Science and Technology **27**, 124003 (2012).
[4] C. W. J. Beenakker, "Search for majorana fermions in superconductors," Annual Review of Condensed Matter Physics **4**, 113–136 (2013).
[5] T. D. Stanescu and S. Tewari, "Majorana fermions in semiconductor nanowires: fundamentals, modeling, and experiment," Journal of Physics: Condensed Matter **25**, 233201 (2013).
[6] S. R. Elliott and M. Franz, "*Colloquium*: Majorana fermions in nuclear, particle, and solid-state physics," Rev. Mod. Phys. **87**, 137–163 (2015).
[7] S. Das Sarma, M. Freedman, and C. Nayak, "Majorana zero modes and topological quantum computation," Npj Quantum Information **1**, 15001 EP – (2015), review Article.
[8] M. Sato and S. Fujimoto, "Majorana fermions and topology in superconductors," Journal of the Physical Society of Japan **85**, 072001 (2016).
[9] R. Aguado, "Majorana quasiparticles in condensed matter," Riv. Nuovo Cim. **40**, 1 (2017).
[10] N. Read and D. Green, "Paired states of fermions in two dimensions with breaking of parity and time-reversal symmetries and the fractional quantum hall effect," Phys. Rev. B **61**, 10267 (2000).
[11] A. Yu. Kitaev, "Unpaired majorana fermions in quantum wires," Physics-Uspekhi **44**, 131 (2001).
[12] D. A. Ivanov, "Non-abelian statistics of half-quantum vortices in p-wave superconductors," Phys. Rev. Lett. **86**, 268–271 (2001).
[13] C. Nayak, S. H. Simon, A. Stern, M. Freedman, and S. Das Sarma, "Non-abelian anyons and topological quantum computation," Rev. Mod. Phys. **80**, 1083–1159 (2008).
[14] P. Bonderson, M. Freedman, and C. Nayak, "Measurement-only topological quantum computation," Phys. Rev. Lett. **101**, 010501 (2008).
[15] P. Bonderson, M. Freedman, and C. Nayak, "Measurement-only topological quantum computation via anyonic interferometry," Annals of Physics **324**, 787 – 826 (2009).
[16] J. D. Sau, S. Tewari, and S. Das Sarma, "Universal quantum computation in a semiconductor quantum wire network," Phys. Rev. A **82**, 052322 (2010).
[17] J.K. Pachos, *Introduction to Topological Quantum Computation* (Cambridge University Press, 2012).
[18] L. Mazza, M. Rizzi, M. D. Lukin, and J. I. Cirac, "Robustness of quantum memories based on majorana zero modes," Phys. Rev. B **88**, 205142 (2013).
[19] T. Hyart, B. van Heck, I. C. Fulga, M. Burrello, A. R. Akhmerov, and C. W. J. Beenakker, "Flux-controlled quantum computation with majorana fermions," Phys. Rev. B **88**, 035121 (2013).
[20] P. Bonderson, "Measurement-only topological quantum computation via tunable interactions," Phys. Rev. B **87**, 035113 (2013).
[21] D. Aasen, M. Hell, R. V. Mishmash, A. Higginbotham, J. Danon, M. Leijnse, T. S. Jespersen, J. A. Folk, C. M. Marcus, K. Flensberg, and J. Alicea, "Milestones toward majorana-based quantum computing," Phys. Rev. X **6**, 031016 (2016).
[22] D. J. Clarke, J. D. Sau, and S. Das Sarma, "A practical phase gate for producing bell violations in majorana wires," Phys. Rev. X **6**, 021005 (2016).
[23] M. Ippoliti, M. Rizzi, V. Giovannetti, and L. Mazza, "Quantum memories with zero-energy majorana modes and experimental constraints," Phys. Rev. A **93**, 062325 (2016).
[24] J. Alicea, Y. Oreg, G. Refael, F. von Oppen, and M. P. A. Fisher, "Non-abelian statistics and topological quantum information processing in 1d wire networks," Nature Physics **7**, 412 EP – (2011), article.
[25] D. J. Clarke, J. D. Sau, and S. Tewari, "Majorana fermion exchange in quasi-one-dimensional networks," Phys. Rev. B **84**, 035120 (2011).
[26] J. D. Sau, D. J. Clarke, and S. Tewari, "Controlling non-abelian statistics of majorana fermions in semiconductor nanowires," Phys. Rev. B **84**, 094505 (2011).
[27] M. Cheng, V. Galitski, and S. Das Sarma, "Nonadiabatic

effects in the braiding of non-abelian anyons in topological superconductors," Phys. Rev. B **84**, 104529 (2011).
[28] A. Romito, J. Alicea, G. Refael, and F. von Oppen, "Manipulating majorana fermions using supercurrents," Phys. Rev. B **85**, 020502 (2012).
[29] B. I. Halperin, Y. Oreg, A. Stern, G. Refael, J. Alicea, and F. von Oppen, "Adiabatic manipulations of majorana fermions in a three-dimensional network of quantum wires," Phys. Rev. B **85**, 144501 (2012).
[30] B. van Heck, A. R. Akhmerov, F. Hassler, M. Burrello, and C. W. J. Beenakker, "Coulomb-assisted braiding of majorana fermions in a josephson junction array," New Journal of Physics **14**, 035019 (2012).
[31] M. Burrello, B. van Heck, and A. R. Akhmerov, "Braiding of non-abelian anyons using pairwise interactions," Phys. Rev. A **87**, 022343 (2013).
[32] M. S. Scheurer and A. Shnirman, "Nonadiabatic processes in majorana qubit systems," Phys. Rev. B **88**, 064515 (2013).
[33] C.-K. Chiu, M. M. Vazifeh, and M. Franz, "Majorana fermion exchange in strictly one-dimensional structures," EPL (Europhysics Letters) **110**, 10001 (2015).
[34] T. Karzig, F. Pientka, G. Refael, and F. von Oppen, "Shortcuts to non-abelian braiding," Phys. Rev. B **91**, 201102 (2015).
[35] C. S. Amorim, K. Ebihara, A. Yamakage, Y. Tanaka, and M. Sato, "Majorana braiding dynamics in nanowires," Phys. Rev. B **91**, 174305 (2015).
[36] B. Bauer, T. Karzig, R. V. Mishmash, A. E. Antipov, and J. Alicea, "Dynamics of Majorana-based qubits operated with an array of tunable gates," ArXiv e-prints (2018), arXiv:1803.05451 [cond-mat.mes-hall].
[37] S. B. Bravyi and A. Yu. Kitaev, "Fermionic quantum computation," Annals of Physics **298**, 210 – 226 (2002).
[38] S. B. Bravyi and A. Yu. Kitaev, "Universal quantum computation with ideal clifford gates and noisy ancillas," Phys. Rev. A **71**, 022316 (2005).
[39] S. B. Bravyi, "Universal quantum computation with the $\nu = 52$ fractional quantum hall state," Phys. Rev. A **73**, 042313 (2006).
[40] L. Fu and C. L. Kane, "Superconducting proximity effect and majorana fermions at the surface of a topological insulator," Phys. Rev. Lett. **100**, 096407 (2008).
[41] Y. Oreg, G. Refael, and F. von Oppen, "Helical liquids and majorana bound states in quantum wires," Phys. Rev. Lett. **105**, 177002 (2010).
[42] R. M. Lutchyn, J. D. Sau, and S. Das Sarma, "Majorana fermions and a topological phase transition in semiconductor-superconductor heterostructures," Phys. Rev. Lett. **105**, 077001 (2010).
[43] V. Mourik, K. Zuo, S. M. Frolov, S. R. Plissard, E. P. A. M. Bakkers, and L. P. Kouwenhoven, "Signatures of majorana fermions in hybrid superconductor-semiconductor nanowire devices," Science **336**, 1003–1007 (2012).
[44] A. Das, Y. Ronen, Y. Most, Y. Oreg, M. Heiblum, and H. Shtrikman, "Zero-bias peaks and splitting in an al-inas nanowire topological superconductor as a signature of majorana fermions," Nature Physics **8**, 887 EP – (2012), article.
[45] I. C. Fulga, A. Haim, A. R. Akhmerov, and Y. Oreg, "Adaptive tuning of majorana fermions in a quantum dot chain," New Journal of Physics **15**, 045020 (2013).
[46] H. O. H. Churchill, V. Fatemi, K. Grove-Rasmussen, M. T. Deng, P. Caroff, H. Q. Xu, and C. M. Marcus, "Superconductor-nanowire devices from tunneling to the multichannel regime: Zero-bias oscillations and magnetoconductance crossover," Phys. Rev. B **87**, 241401 (2013).
[47] A. D. K. Finck, D. J. Van Harlingen, P. K. Mohseni, K. Jung, and X. Li, "Anomalous modulation of a zero-bias peak in a hybrid nanowire-superconductor device," Phys. Rev. Lett. **110**, 126406 (2013).
[48] S. Nadj-Perge, I. K. Drozdov, J. Li, H. Chen, S. Jeon, J. Seo, A. H. MacDonald, B. A. Bernevig, and A. Yazdani, "Observation of majorana fermions in ferromagnetic atomic chains on a superconductor," Science **346**, 602–607 (2014).
[49] S. M. Albrecht, A. P. Higginbotham, M. Madsen, F. Kuemmeth, T. S. Jespersen, J. Nygård, P. Krogstrup, and C. M. Marcus, "Exponential protection of zero modes in majorana islands," Nature **531**, 206 EP – (2016).
[50] M. T. Deng, S. Vaitiekenas, E. B. Hansen, J. Danon, M. Leijnse, K. Flensberg, J. Nygård, P. Krogstrup, and C. M. Marcus, "Majorana bound state in a coupled quantum-dot hybrid-nanowire system," Science **354**, 1557–1562 (2016).
[51] M. T. Deng, S. Vaitiekénas, E. Prada, P. San-Jose, J. Nygård, P. Krogstrup, R. Aguado, and C. M. Marcus, "Majorana non-locality in hybrid nanowires," ArXiv e-prints (2017), arXiv:1712.03536 [cond-mat.mes-hall].
[52] R. M. Lutchyn, E. P. A. M. Bakkers, L. P. Kouwenhoven, P. Krogstrup, C. M. Marcus, and Y. Oreg, "Realizing Majorana zero modes in superconductor-semiconductor heterostructures," ArXiv e-prints (2017), arXiv:1707.04899 [cond-mat.supr-con].
[53] T.-P. Choy, J. M. Edge, A. R. Akhmerov, and C. W. J. Beenakker, "Majorana fermions emerging from magnetic nanoparticles on a superconductor without spin-orbit coupling," Phys. Rev. B **84**, 195442 (2011).
[54] S. Nadj-Perge, I. K. Drozdov, B. A. Bernevig, and Ali Yazdani, "Proposal for realizing majorana fermions in chains of magnetic atoms on a superconductor," Phys. Rev. B **88**, 020407 (2013).
[55] J. Klinovaja, P. Stano, A. Yazdani, and D. Loss, "Topological superconductivity and majorana fermions in rkky systems," Phys. Rev. Lett. **111**, 186805 (2013).
[56] S. Nadj-Perge, I. K. Drozdov, J. Li, H. Chen, S. Jeon, J. Seo, A. H. MacDonald, B. A. Bernevig, and A. Yazdani, "Observation of majorana fermions in ferromagnetic atomic chains on a superconductor," Science **346**, 602–607 (2014).
[57] M. Ruby, F. Pientka, Y. Peng, F. von Oppen, B. W. Heinrich, and K. J. Franke, "End states and subgap structure in proximity-coupled chains of magnetic adatoms," Phys. Rev. Lett. **115**, 197204 (2015).
[58] R. Pawlak, M. Kisiel, J. Klinovaja, T. Meier, S. Kawai, T. Glatzel, D. Loss, and E. Meyer, "Probing atomic structure and majorana wavefunctions in mono-atomic fe chains on superconducting pb surface," NPJ Quantum Information **2**, 16035 (2016).
[59] B. E. Feldman, M. T. Randeria, J. Li, S. Jeon, Y. Xie, Z. Wang, I. K. Drozdov, B. A. Bernevig, and A. Yazdani, "High-resolution studies of the majorana atomic chain platform," Nature Physics **13**, 286–291 (2017).
[60] M. Hell, M. Leijnse, and K. Flensberg, "Two-dimensional platform for networks of majorana bound states," Phys. Rev. Lett. **118**, 107701 (2017).
[61] M. Hell, K. Flensberg, and M. Leijnse, "Coupling and braiding majorana bound states in networks defined in

two-dimensional electron gases with proximity-induced superconductivity," Phys. Rev. B **96**, 035444 (2017).
[62] J. D. Sau, S. Tewari, and S. Das Sarma, "Probing non-abelian statistics with majorana fermion interferometry in spin-orbit-coupled semiconductors," Phys. Rev. B **84**, 085109 (2011).
[63] S. Das Sarma, A. Nag, and J. D. Sau, "How to infer non-abelian statistics and topological visibility from tunneling conductance properties of realistic majorana nanowires," Phys. Rev. B **94**, 035143 (2016).
[64] D. J. Clarke, "Experimentally accessible topological quality factor for wires with zero energy modes," Phys. Rev. B **96**, 201109 (2017).
[65] E. Prada, R. Aguado, and P. San-Jose, "Measuring majorana nonlocality and spin structure with a quantum dot," Phys. Rev. B **96**, 085418 (2017).
[66] C.-X. Liu, J. D. Sau, T. D. Stanescu, and S. Das Sarma, "Andreev bound states versus majorana bound states in quantum dot-nanowire-superconductor hybrid structures: Trivial versus topological zero-bias conductance peaks," Phys. Rev. B **96**, 075161 (2017).
[67] A. Ptok, A. Kobiałka, and T. Domański, "Controlling the bound states in a quantum-dot hybrid nanowire," Phys. Rev. B **96**, 195430 (2017).
[68] A. Schuray, L. Weithofer, and P. Recher, "Fano resonances in majorana bound states˘quantum dot hybrid systems," Phys. Rev. B **96**, 085417 (2017).
[69] C.-X. Liu, J. D. Sau, and S. Das Sarma, "Distinguishing topological Majorana bound states from trivial Andreev bound states: Proposed tests through differential tunneling conductance spectroscopy," ArXiv e-prints (2018), arXiv:1803.05423.
[70] D. Chevallier, P. Szumniak, S. Hoffman, D. Loss, and J. Klinovaja, "Topological phase detection in rashba nanowires with a quantum dot," Phys. Rev. B **97**, 045404 (2018).
[71] K. Gharavi, D. Hoving, and J. Baugh, "Readout of majorana parity states using a quantum dot," Phys. Rev. B **94**, 155417 (2016).
[72] In fact, $\hat{P}^{(H)}(t) = i\hat{\gamma}_1(t)\hat{\gamma}_2(t)\hat{\gamma}'(t)$ is not the fermionic parity. Nonetheless the same proof holds if one replaces it with the true parity operator $\hat{P}_2^{(H)}(t) = -\hat{\gamma}_0(t)\hat{\gamma}_1(t)\hat{\gamma}_2(t)\hat{\gamma}'(t)$ as $\hat{\gamma}_0(t)$ commutes with the Hamiltonian at all times.
[73] MZMs $\hat{\gamma}_1$ and $\hat{\gamma}_2$ are actually connected to the network through three couplings that could be called $\eta_{j,1}$ and $\eta_{j,2}$, $j = 1\ldots3$, similarly to the simpler case shown in Fig. 4, panel c). For simplicity, we only denote them as η_1 and η_2, the relevant question being whether the couplings are *on* or *off* and not the number of links.
[74] D. J. Clarke, J. D. Sau, and S. Das Sarma, "Probability and braiding statistics in majorana nanowires," Phys. Rev. B **95**, 155451 (2017).
[75] W. G. van der Wiel, S. De Franceschi, J. M. Elzerman, T. Fujisawa, S. Tarucha, and L. P. Kouwenhoven, "Electron transport through double quantum dots," Rev. Mod. Phys. **75**, 1–22 (2002).
[76] R. Hanson, L. P. Kouwenhoven, J. R. Petta, S. Tarucha, and L. M. K. Vandersypen, "Spins in few-electron quantum dots," Rev. Mod. Phys. **79**, 1217–1265 (2007).
[77] Y. Hu, H. O. H. Churchill, D. J. Reilly, J. Xiang, C. M. Lieber, and C. M. Marcus, "A ge/si heterostructure nanowire-based double quantum dot with integrated charge sensor," Nature Nanotechnology **2**, 622 EP – (2007).
[78] C. Barthel, D. J. Reilly, C. M. Marcus, M. P. Hanson, and A. C. Gossard, "Rapid single-shot measurement of a singlet-triplet qubit," Phys. Rev. Lett. **103**, 160503 (2009).
[79] F. Persson, C. M. Wilson, M. Sandberg, and P. Delsing, "Fast readout of a single cooper-pair box using its quantum capacitance," Phys. Rev. B **82**, 134533 (2010).
[80] K. D. Petersson, C. G. Smith, D. Anderson, P. Atkinson, G. A. C. Jones, and D. A. Ritchie, "Charge and spin state readout of a double quantum dot coupled to a resonator," Nano Letters **10**, 2789–2793 (2010).
[81] Y. Hu, F. Kuemmeth, C. M. Lieber, and C. M. Marcus, "Hole spin relaxation in ge-si core-shell nanowire qubits," Nature Nanotechnology **7**, 47 EP – (2011).
[82] M. Jung, M. D. Schroer, K. D. Petersson, and J. R. Petta, "Radio frequency charge sensing in inas nanowire double quantum dots," Applied Physics Letters **100**, 253508 (2012), https://doi.org/10.1063/1.4729469.
[83] J. Medford, J. Beil, J. M. Taylor, S. D. Bartlett, A. C. Doherty, E. I. Rashba, D. P. DiVincenzo, H. Lu, A. C. Gossard, and C. M. Marcus, "Self-consistent measurement and state tomography of an exchange-only spin qubit," Nature Nanotechnology **8**, 654 EP – (2013), article.
[84] J. I. Colless, A. C. Mahoney, J. M. Hornibrook, A. C. Doherty, H. Lu, A. C. Gossard, and D. J. Reilly, "Dispersive readout of a few-electron double quantum dot with fast rf gate sensors," Phys. Rev. Lett. **110**, 046805 (2013).
[85] K. Eng, T. D. Ladd, A. Smith, M. G. Borselli, A. A. Kiselev, B. H. Fong, K. S. Holabird, T. M. Hazard, B. Huang, P. W. Deelman, I. Milosavljevic, A. E. Schmitz, R. S. Ross, M. F. Gyure, and A. T. Hunter, "Isotopically enhanced triple-quantum-dot qubit," Science Advances **1** (2015), 10.1126/sciadv.1500214.
[86] J. Stehlik, Y.-Y. Liu, C. M. Quintana, C. Eichler, T. R. Hartke, and J. R. Petta, "Fast charge sensing of a cavity-coupled double quantum dot using a josephson parametric amplifier," Phys. Rev. Applied **4**, 014018 (2015).
[87] B. Trauzettel, A. N. Jordan, C. W. J. Beenakker, and M. Büttiker, "Parity meter for charge qubits: An efficient quantum entangler," Phys. Rev. B **73**, 235331 (2006).
[88] M. D. Schroer, M. Jung, K. D. Petersson, and J. R. Petta, "Radio frequency charge parity meter," Phys. Rev. Lett. **109**, 166804 (2012).
[89] D. Gottesman, "The Heisenberg Representation of Quantum Computers," eprint arXiv:quant-ph/9807006 (1998), quant-ph/9807006.
[90] S. B. Bravyi and J. Haah, "Magic-state distillation with low overhead," Phys. Rev. A **86**, 052329 (2012).
[91] A. M. Meier, B. Eastin, and E. Knill, "Magic-state distillation with the four-qubit code," ArXiv e-prints (2012), arXiv:1204.4221 [quant-ph].
[92] A. Paetznick and B. W. Reichardt, "Universal fault-tolerant quantum computation with only transversal gates and error correction," Phys. Rev. Lett. **111**, 090505 (2013).
[93] C. Jones, "Low-overhead constructions for the fault-tolerant toffoli gate," Phys. Rev. A **87**, 022328 (2013).
[94] B. Eastin, "Distilling one-qubit magic states into toffoli states," Phys. Rev. A **87**, 032321 (2013).